RANS CFD METHODOLOGIES FOR A PWR FUEL ROD ASSEMBLY

A Thesis

by

THEODORE NICHOLAS BLOWE

Submitted to the Office of Graduate and Professional Studies of
Texas A&M University
in partial fulfillment of the requirements for the degree of

MASTER OF SCIENCE

Chair of Committee,	Yassin Hassan
Committee Members,	Nagamangala Anand
	William Marlow
Head of Department,	Andreas Polycarpou

December 2015

Major Subject: Mechanical Engineering

ABSTRACT

This study adopts computational fluid dynamics (CFD) to examine fluid dynamics and heat transfer characteristics for turbulent flows around pressurized water reactor (PWR) fuel rod bundles with support grids. The NESTOR experiment performed by CEA-EDF-EPRI provided accurate data for various variables (mean and RMS axial velocities, pressure drops, and rod inner-surface temperatures) for a 5×5 PWR fuel rod assembly with and without complex split-type mixing vane grids (MVGs).

This study investigates isolated CFD methodological factors for rod bundles with complex split-type MVGs under isothermal and single-phase heated prototypic PWR thermal hydraulic conditions. Examined CFD methodological factors include; mesh size, isotropic/anisotropic turbulence models, axial domain considerations, and conjugate heat transfer considerations for the single-phase heated problem. Reynolds Averaged Navier-Stokes (RANS) turbulence models were considered because of their practical feasibility in application to the real PWR fuel rod bundle.

Under a high-quality mesh, results from isothermal steady calculations adopted steady RANS turbulence models with a wall function (high-y+ treatment) can produce; (i) accurate pressure losses across MVG and SSG spans, (ii) comparable mean axial velocity (MVG and simple support grid (SSG) spans), and (iii) comparable and RMS axial velocity fluctuation (MVG span) profiles with NESTOR experimental profiles for

the MVG rod bundle with alternating SSGs in the downstream regions. Heated steady calculations over-predicted axial and azimuthal rod inner-surface temperature distributions at various axial elevations in the MVG and SSG span wake region.

DEDICATION

To my Father, Mother, and Siblings

To Dr. Shin K. Kang

ACKNOWLEDGEMENTS

I would like to thank my committee chair, Dr. Yassin Hassan, and my committee members, Dr. Nagamangala Anand, and Dr. William Marlow, for their guidance and support throughout the course of this study.

I also want to thank my friends, colleagues, and the department faculty and staff for making my time at Texas A&M University a great experience. I extend my gratitude to the Texas A&M University Nuclear Engineering Department and EPRI, for funding this research project.

TABLE OF CONTENTS

Page

LIST OF FIGURES

Page

LIST OF TABLES

Page

1 INTRODUCTION

1.1 Background

In recent years, advances in PWR fuel performance have led to higher fuel burnup, longer fuel cycles, and power uprates. Demonstrating fuel reliability under these enhanced conditions is a key challenge for high-duty PWR cores. Failure to do so may increase shutdown frequency and limit operational freedom. Fuel failures and unexpected power shifts during operations are fuel reliability risk factors. A possible fuel failure mechanism and undesirable power shift mechanism are the occurrence of (i) crud-induced localized corrosion (CILC), and (ii) crud-induced power shift (CIPS previously called Axial Offset Anomaly), respectively. Sub-cooled nucleate boiling (SNB) in the upper region of a PWR core is known to facilitate the build-up of corrosion products on fuel rod surfaces. Understanding local fuel rod bundle conditions is a necessary step for mitigating risk associated with CILC induced fuel failures and CIPS incidents.

A collection of fuel assemblies arranged in a square array pattern forms a typical PWR core. Common PWR fuel assemblies span approximately four meters in height, and consist of an in-line 17×17 square array of fuel rods with constant pitch spacing between adjacent rods. Fuel rods are held in place by support grids placed along the fuel assembly. Support grids with mixing vanes at the end of grid straps, commonly referred to as MVGs; enhance turbulent mixing along the MVG wake region. Enhanced turbulent mixing helps prevent the occurrence of SNB by increasing the critical heat flux (CHF).

Studying fluid dynamics and single-phase heat transfer characteristics for turbulent flows around PWR fuel rod bundles with complex split-type MVGs is crucial to predict local hot spots, i.e. potential SNB regions. Neither one dimensional system codes, nor sub-channel codes appropriately predict local hot spots. In contrast, CFD codes can analyze and resolve turbulent flow structures and local heat transfer characteristics regarding a PWR fuel rod bundle. These CFD codes must be validated prior to practical thermal hydraulic application.

1.2 Previous works

Previous works studying local axial and lateral flow structures and behavior for square arranged rod bundle at various split-type MVG –near, intermediate, and far- wakes regions are discussed, as shown in Table 1.

Table 1 Rod Bundle with split-type MVG Experiments (chronological order)

Author	Bundle Array	Operating Conditions	Grid Type	Measurements	Measurement Locations (z/D_h)
Herr and Pröbstle [1]	2×2 array square horizontal	isothermal, Re ≈2,000 – 60,000	Split-vane	Mean axial and tangential velocities	Center sub-channel, 4 axial elevations (0.3, 0.7, 1.0, and 1.5)
Karoutas and Schölin [2]	5×5 array square	isothermal, Re ≈89,500	Split-vane	Mean axial and lateral velocities	Two adjacent interior sub-channels, 7 axial locations (1,2,4,8,15,25,36)
McClusky et al. [3]	5×5 array square vertical	isothermal, Re ≈28,000	Split-vane pairs	Lateral full-field velocity	Four central sub-channels, 7 axial locations (1.4-17)
Chang et al. [4]	5×5 array square vertical	isothermal, Re ≈48,000	Split-vane, swirl	Pressure drop, mean axial and lateral velocity, turbulent intensity	6 axial elevations (1,2,4,8,16,71)
Yang and Chang [5]	5×5 array square horizontal	isothermal, Re ≈62,500	Split-vane	Pressure drop, mean axial velocity and turbulence intensity	Quarter lateral domain ,6 axial elevations (2, 4, 8, 16, 32, 50)
Shen et al. [6]	4×4 array square vertical	isothermal, Re ≈14,200	Mixing-blades	Lateral mean and RMS velocity	Center sub-channel and rod gap spacing, 9 axial locations (5-45)

Even though a typical PWR operates at high Reynold's numbers, $\mathrm{Re} \approx 500{,}000$, Herr and Pröbstle [1] show similar normalized axial and lateral velocity profiles in the near wake region for $\mathrm{Re} \approx 2{,}000 - 60{,}000$. Axial and lateral velocity profiles in the near wake region may be independent of Reynold's number, and may be qualitatively similar between low and high Reynold's numbers. Velocity profile dependence on Reynold's number in the intermediate and far wake regions was not examined. At the beginning of the vanes, Herr and Pröbstle [1] observed the presence of large and small axial velocity contours in-between; vane and rod wall gap region; rod wall and open gap region (oriented 90° from largest magnitude axial velocity contour), respectively. Herr and Pröbstle [1] suggest flow separating at the rod wall may cause the lateral migration of axial velocity contours. This suggestion motivates the possible presence of large scale coherent unsteady vortex interactions in the near wake region.

At the vane tips, strong swirling flow is similar to that of the well documented Rankine vortex (Herr and Pröbstle [1]). Furthermore, lateral velocity component constitutes about 30% of the bulk axial velocity, and axial velocity locally peaks in gap region adjacent to the vane (Herr and Pröbstle [1], and Karoutas and Schölin [2]). At 1.4 z/D_h two pairs of vortices are present near each vane region for a total of four vortices for each examined sub-channel (McClusky et al. [3]). One vortex is shed from the vane knee (knee vortex). One vortex is shed from the vane tip, referred to as tip vortex (McClusky et al. [3] and Chang et al. [4]). The two tip vortices form a co-rotating pair vortex located in the central sub-channel region as about one fourth of the pitch (McClusky et al. [3] and

Chang et al [4]). Knee vortices parallel to vane-pair orientation are located between adjacent rods in the narrow gap region (McClusky et al. [3]). Depending on sub-channel location; knee vortices dissipate completely at either 2.8 z/D_h or 4.2 z/D_h (McClusky et al. [3]). Likewise, the co-rotating tip vortex pair dissipate, or form a single vortex by 4.2 z/D_h (McClusky et al. [3] and Chang et al. [4]). Chang et al. [4] states that cross-flow in the gap regions is the main contributor to energy exchange between sub-channels.

From 6.3 to 17.0 z/D_h, a single circular vortex is present from either; (i) dissipation one of the tip vortices, or (ii) the two tip vortices merge into one (McClusky et al. [3]). As the flow evolves in the axial direction, the single vortex laterally migrates within the sub-channel. Spring and dimple effects may cause hairpin type flow structure observed in axial direction for some sub-channels.

Axial and lateral velocity fluctuations decrease as the flow progresses downstream from the MVG (Chang et al. [4]). The axial velocity profile of interior sub-channels is almost flat 8 hydraulic diameters downstream of the grid and beyond (Yang and Chang [5] and Chang et al. [4]). Axial velocity increases in the central sub-channel region and decreasing axial velocity in the gap region from 16 to 50 hydraulic diameters downstream of the grid. Axial velocity reaches a nearly fully developed condition 32 and 50 hydraulic diameters downstream of the grid. In this far wake region, axial turbulent intensity is lower in the sub-channel center compared to the gap region.

Shen et al. [6] examines how vane angle impacts mixing rate intensity and axial location of velocity inversion in the grid wake region. Increasing vane angle increases mixing rate (swirl flow). The larger vane angle may have more intense swirl flow, but swirl flow rapidly decreases in the axial direction. Shen et al. [6] describes how the test section housing walls directly affected the lateral flow field as a function of vane angle. Karoutas and Schölin [2] shows a clear difference in local axial velocity maxima and minima location between adjacent interior sub-channels between 1.0 and 2.0 z/D_h. At 1.0 z/D_h local axial velocity maxima found near gap region, and local minima found near sub-channel center (Karoutas and Schölin [2]). At 2.0 z/D_h and beyond, one of the two measured sub-channels local axial velocity maxima located near sub-channel center, and local minima measured near gap region (Karoutas and Schölin [2]). Yang and Chang [5] compare the difference in axial velocity profiles as a function of axial distance from MVG and lateral distance from test section wall. Axial velocity profiles near housing wall/corner sub-channels (18, 32, 50 z/D_h) are flatter than axial velocity profiles for interior sub-channels closer to the center of the rod bundle.

The availability of discussed experimental results provides a platform for validating CFD codes and methodologies. Experimental test sections smaller than a 5×5 square array are not considered in the CFD-code-to-experiment literature review.

Conner et al. [7] adopts the following CFD methodologies; steady RANS turbulence model (RNG k-ε by Yakhot et al. [8]), trim type mesh, and uniform inlet velocity with

split-flow outlet velocity under steady-state single-phase heated thermal hydraulic conditions with complex split-type MVG. Conner et al. [7] compares calculated mean lateral flow velocity vector profiles 50 mm downstream of the MVG with measured values from McClusky et al. [3].

Lee et al. [9] synthesizes CFD calculations submitted from twenty-five participants for the Second International Benchmark Exercise (IBE-2). IBE-2 adopted the experimental facility described by Chang et al. [4] under isothermal operating conditions, $\mathrm{Re} \approx 50{,}250$. The majority of participants for IBE-2 adopted unsteady temporal considerations in order to capture strong transient behavior of the large scale vortex shedding fluctuations from the vanes in the wake regions (Lee et al. [9]).

1.3 Motivation

Previous works may characterize local fluid structures and flow behavior at various wake regions for a fuel rod bundle with split-type MVG, but do not describe rod surface temperature along the MVG wake region. This motivates the need for additional experiments and associated CFD-code-to-experiment benchmarks. In the outlined framework, and the CEA-EDF-EPRI collaborative NESTOR project, Bergeron et al. [10] and EPRI [11], aimed to produce accurate thermal-hydraulic experimental data for 5×5 rod bundles with support grids at prototypic PWR thermal hydraulic conditions. Characterization of grid pressure loss and axial velocity fields by Laser-Doppler Velocimetry (LDV) in single-phase flow was examined during hydraulic isothermal tests

on the EDF-CHATOU MANIVEL loop. Axially sliding and rotating thermocouple probes inside the rods measured rod inner-surface temperature during heated single-phase and onset nucleate boiling (ONB) tests on the CEA-GRENOBLE OMEGA loop. This study adopted high fidelity experimental measurements from the CEA-EDF-EPRI collaborative NESTOR project for isothermal and single-phase heated CFD-code-to-experiment benchmark comparisons.

1.4 Objective

The objective of this study is to validate adopted CFD methodologies (mesh characteristics, axial computational domain selection, turbulence models, steady/unsteady temporal numerical schemes, and conjugate heat transfer considerations) with high fidelity experimental data for 5×5 rod bundles with split-type MVGs of the Westinghouse V5H design under prototypic PWR isothermal and single-phase heated thermal hydraulic conditions. This study adopted the commercial software Star-CCM+ v9.04.009 from CD-adapco, which uses a finite volume approach to solve the RANS equations.

2 PROBLEM SPECIFICATION (NESTOR EXPERIMENTS)

This section describes the domain characteristics, thermal hydraulic test conditions, and measurement information regarding the MANIVEL MVG and OMEGA MVG bundle experiments required for CFD-to-experiment benchmark calculations. A detailed description of the NESTOR experiments with associated CFD round robin benchmark is explained by EPRI [11].

2.1 Geometry

The MANIVEL MVG and OMEGA MVG rod bundles have similar global domain characteristics, as described in Table 2 and shown in Figure 1 by EPRI [11]. Both rod bundles are arranged in a 5×5 square array pattern with lateral cross sectional range of $0.0661m\times0.0661m$. Similarly, each bundle spans a total axial length of approximately $5m$, while the heated axial length of the OMEGA MVG bundle is $3.658m$. The rod outer diameter, rod to rod pitch, and rod to wall gap lengths are $0.0095m$, $0.0126m$, and $0.0031m$, respectively. The test section hydraulic diameter accounts for the total wetted perimeter and cross sectional area of the lateral bundle domain.

Alternating MVGs of the Westinghouse V5H design and SSGs were adopted as support grids in the NESTOR MVG bundle experiments, as shown in Figure 2. The adopted MVGs in this study can be decomposed into two axial components; (i) spacer grid, and (ii) mixing vanes. The MVG spacer grid consists of grid straps, spring, and dimples.

Spring and dimples hold the rods in place and prevent excessive rod vibration. Furthermore, either a singular spring or pair of dimples obscures fluid flow directly upstream of the mixing vanes, as shown in Figure 3. SSGs were adopted for this study to provide additional support in-between MVG spans. The SSG design adopted in the MANIVEL MVG and OMEGA MVG bundles do not exist in actual PWR cores.

A total of three MVG orientations were adopted for the NESTOR MVG bundles; MANIVEL MVG01, OMEGA MVG01, and MVG02, as shown in Table 3 by EPRI [11]. This study obtained MANIVEL MVG01 orientation from the clockwise rotation of MVG02 orientation by 90° about the z-axis. However, OMEGA MVG01 orientation was obtained from the counter-clockwise rotation of MVG02 orientation by 90° about the z-axis. It should be noted that MVG01 mixing vane orientation is the same for both MANIVEL MVG and OMEGA MVG bundles. The only orientation difference between MANIVEL MVG01 and OMEGA MVG01 is the 180° rotation about the z-axis of spring and dimples located upstream of the mixing vanes.

Table 2 Domain characteristics of NESTOR MVG bundles.

Parameter	Label	Value	Unit
Rod bundle array	_	5×5	_
Lateral domain	_	0.0661×0.0661	$m\times m$
Total length	h_{total}	~ 5	m
Heated length (OMEGA)	h_{heated}	3.658	m
Rod outer diameter	d	0.0095	m
Rod to rod pitch	d_p	0.0126	m
Rod to wall gap	d_g	0.0031	m
Test section hydraulic diameter	d_h	0.0103	m

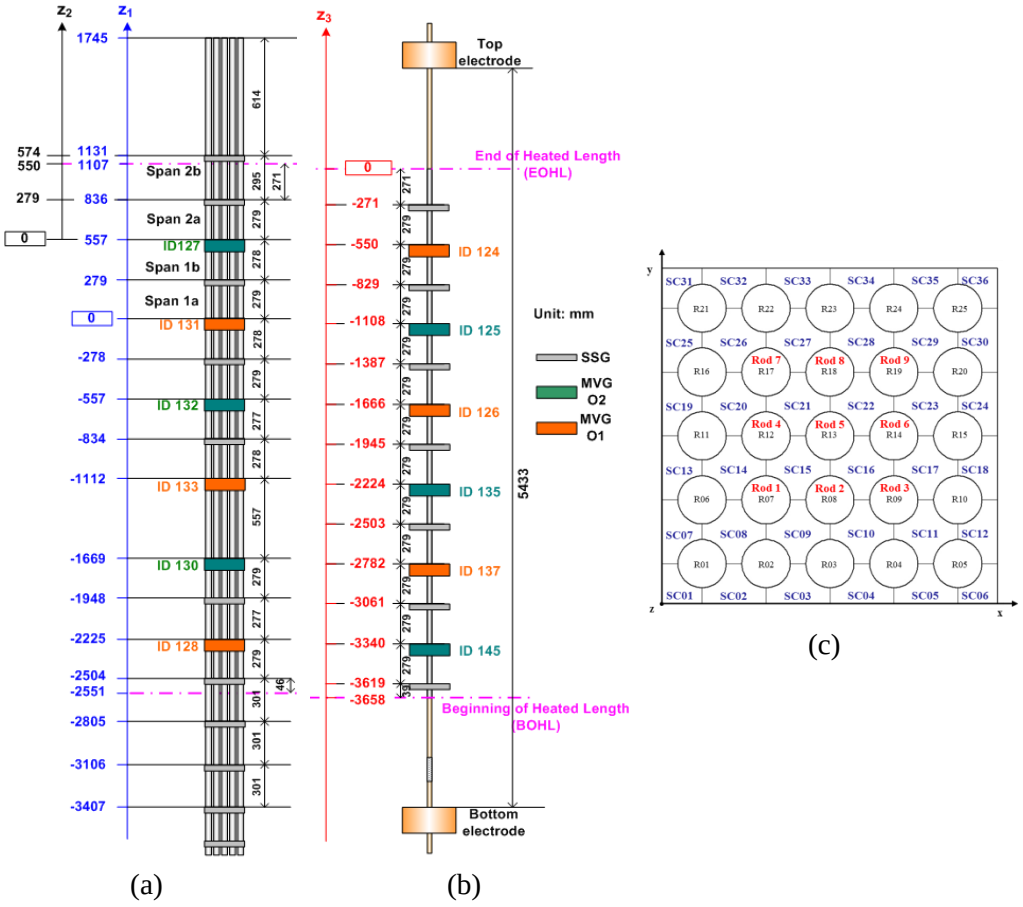

Figure 1 Axial configuration of NESTOR MVG bundles (length in mm); (a) MANIVEL MVG bundle, and (b) OMEGA MVG bundle, reprinted with permission EPRI [11]. Lateral configuration: (c) Sub-channel labels (blue) and measured heated rod labels (red).

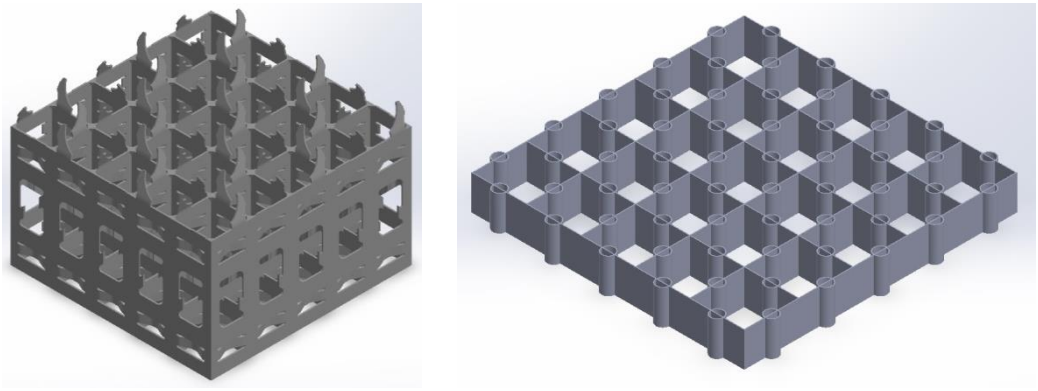

(a) (b)

Figure 2 3D view of support grids: (a) Westinghouse V5H MVG, and (b) SSG.

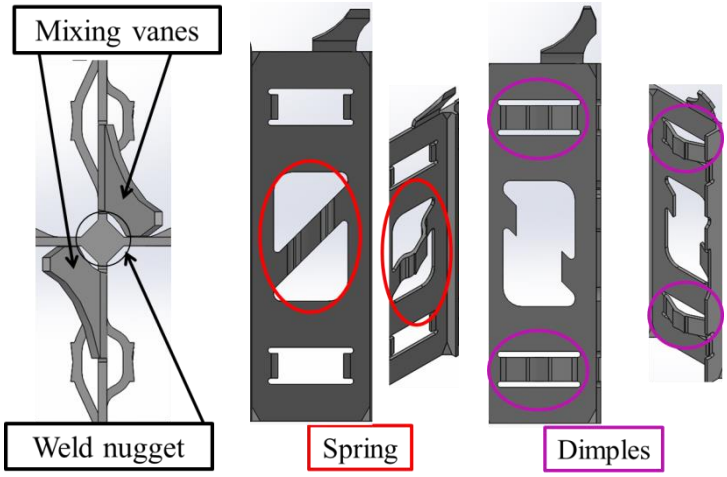

(a) (b) (c)

Figure 3 3D cross-section views of Westinghouse V5H MVG: (a) complex split-type mixing vanes with weld nugget, (b) spring, and (c) dimples.

Table 3 Westinghouse V5H MVG orientations, reprinted with permission EPRI [11]

Label	MANIVEL	OMEGA
MVG01	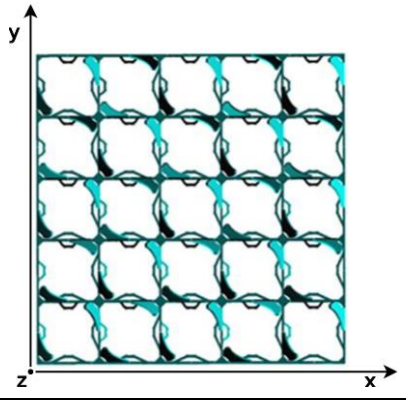	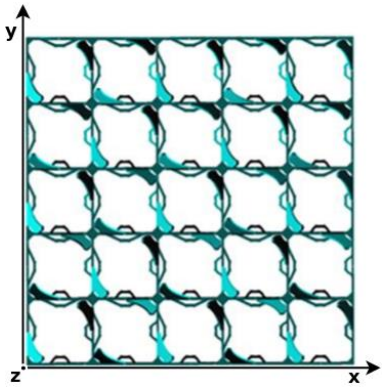
MVG02	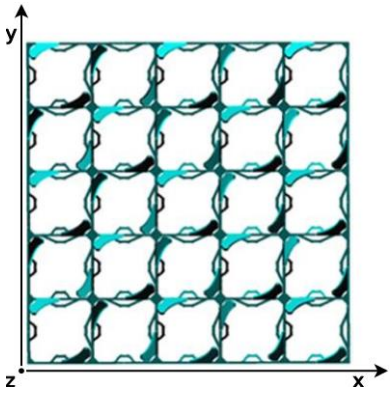	

2.2 Thermal hydraulic test conditions and material properties

2.2.1 MANIVEL-MVG bundle: isothermal experiment

Table 4 presents thermal hydraulic operating conditions, EPRI [11], and fluid properties, Lemmon et al. [12], for the single-phase isothermal test performed on the MANIVEL MVG bundle. The following fluid properties and flow boundary conditions were adopted for CFD-code-to-experiment comparisons; (i) fluid density of $995.74\ kg/m^3$, (ii) fluid dynamic viscosity of $8.0246\times10^{-4}\ Pa\cdot s$, (iii) volumetric flow rate of $64.7\ m^3/h$,

(iv) inlet temperature of $29.7\ °C$, and (v) outlet pressure of $1\ bar$. The associated mean axial velocity and Reynolds number based on d_h are 6.901 and $88{,}320$, respectively.

Table 4 MANIVEL MVG bundle: isothermal (Exercise 1-post) thermal hydraulic test conditions and physical properties, EPRI [11] and Lemmon et al. [12]

Parameter	Label	Value	Unit
Density	ρ_{fluid}	995.74	kg/m^3
Dynamic viscosity	μ_{fluid}	8.0246×10^{-4}	$Pa\cdot s$
Volumetric flow rate	Q	64.7	m^3/h
Mean axial velocity	V_0	6.901	m/s
Inlet temperature	T_{inlet}	29.7	$°C$
Outlet absolute pressure	P_{outlet}	~1	bar
Reynolds number	Re	88,320	_

2.2.2 OMEGA-MVG bundle: heated experiment

EPRI [11] describes thermal hydraulic operating conditions for the single-phase heated test (Run 4-1) performed on the OMEGA MVG bundle, as shown in Table 5. The following boundary conditions were adopted for CFD-code-to-experiment comparisons; (i) mass flux of $3520\ kg/(m^2\cdot s)$, (ii) inlet temperature of $271.1\ °C$, and (ii) outlet absolute pressure of $155.7\ bar$. The associated inlet mean axial velocity and Reynolds number based on d_h are 4.516 and $362{,}415$, respectively.

The rods were heated by passing an electric current through the rods, commonly referred to as Joule heating. Accordingly, the rod cladding acts as a volumetric heat source, as described in Table 6. The following heating power distributions applied to the solid rod cladding regions were adopted for CFD-code-to-experiment comparisons; (i) uniform

volumetric heat flux of $1.073215399\times10^{6}\ kW/m^{3}$ for 9 inner rods labelled Rods 1-9, and (ii) uniform volumetric heat flux of $1.070029050\times10^{6}\ kW/m^{3}$ for the remaining 16 peripheral rods, as shown in Figure 1(c). Table 7 presents fluid and rod material properties for the single-phase heated test performed on the OMEGA MVG bundle, Lemmon et al. [12] and Daw et al. [13], respectively. Stated material properties were interpolated as a function of temperature.

Table 5 OMEGA MVG bundle (Exercise 2-1-post) thermal hydraulic test conditions, EPRI [11]

Parameter	Label	Value	Unit
Mass Flux	G	3520	$kg/(m^2\cdot s)$
Inlet temperature	T_{inlet}	271.1	$°C$
Outlet absolute pressure	P_{outlet}	155.7	bar
Inlet mean axial velocity	V_0	4.516	m/s
Inlet Reynolds number	Re	362,415	_

Table 6 OMEGA MVG bundle (Exercise 2-1-post) heated rod conditions, EPRI [11]

Parameter	Label	Value	Unit
Heated length	h	3.658	m
Inner rod: inner-diameter	$d_{inner_{ID}}$	0.00770	m
Peripheral rod: inner-diameter	$d_{peri_{ID}}$	0.00815	m
Inner rod heated length volume	Vol_{inner}	8.8948×10^{-5}	m^3
Peripheral rod heated length volume	Vol_{peri}	6.8456×10^{-5}	m^3
Total heating power	W_t	2031	kW
Inner rod heating power (9 inner rods)	W_{inner}	95.46	kW
Peripheral rod heating power (16 peripheral rods)	W_{peri}	73.25	kW
Inner rod volumetric heat flux	Q''_{inner}	$\sim1.073\times10^{6}$	kW/m^3
Peripheral rod volumetric heat flux	Q''_{peri}	$\sim1.070\times10^{6}$	kW/m^3

Table 7 OMEGA MVG bundle (Exercise 2-1-post) physical properties (temperature T in °C), Lemmon et al. [12] and Daw et al. [13]

Parameter	Label	Value	Unit
Density	ρ_{fluid}	$-5.1182\times10^{1}+7.3263T-1.5764\times10^{-2}T^{2}$	$\frac{kg}{m^3}$
	ρ_{rod}	8470.0	
Dynamic viscosity	μ_{fluid}	$8.7262\times10^{-4}-7.1286\times10^{-6}T$ $+2.2672\times10^{-8}T^{2}-2.5408\times10^{-11}T^{3}$	$Pa\cdot s$
Thermal conductivity	k_{fluid}	$2.80\times10^{-1}+3.70\times10^{-3}T-9.40\times10^{-6}T^{2}$	$\frac{W}{(m\cdot°C)}$
	k_{rod}	$1.2191\times10^{1}+1.7119\times10^{-2}T+1.2247\times10^{-6}T^{2}$	
Specific heat	$c_{p\ fluid}$	$3.0339\times10^{6}-4.0836\times10^{4}T+206.3T^{2}$ $-0.463T^{3}+3.90\times10^{-4}T^{4}$	$\frac{J}{(kg\cdot°C)}$
	$c_{p\ rod}$	$393+1.3T-8.06\times10^{-3}T^{2}+2.7\times10^{-5}T^{3}$ $+4.42\times10^{-8}T^{4}+2.75\times10^{-11}T^{5}$	

2.3 Experimental measurements

2.3.1 MANIVEL-MVG bundle: isothermal experiment

CFD-code-to-experiment benchmark comparisons for the isothermal MANVEL MVG bundle test consist of grid-span pressure loss and axial velocity fields, as shown in Table 8. Cross-sectional-averaged pressure profiles along MVG and SSG spans were compared. Mean axial velocity and RMS axial velocity fluctuation vector line profiles traversing parallel to spring and dimple features at various axial elevations were examined, as shown in Figure 4. The reference LDV target measurement mesh in each cross-section consisted of approximately 1908 locations (EPRI [11]). Mean axial velocity point measurements were grouped and averaged at each elevation and interior sub-channel ID. Wall and corner sub-channels had inconsistent and missing measurement locations in contrast to interior sub-channels. Thus, mean axial velocity

measurements corresponding to wall and corner sub-channel locations were not adopted for CFD-code-experiment comparisons.

Table 8 MANIVEL-MVG bundle: CFD-code-experiment variables; axial and lateral measurement ranges, reprinted with permission EPRI [11].

<table>
<tr><th>Variables</th><th>Axial range</th><th>Lateral range</th></tr>
<tr><td></td><td> 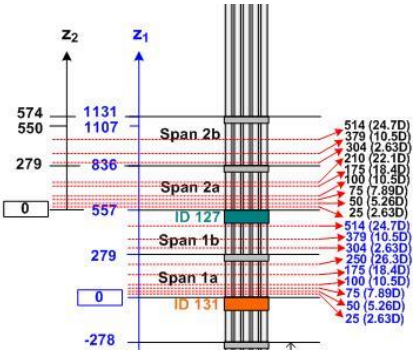
</td><td> 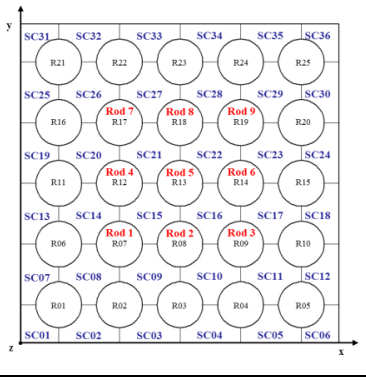
</td></tr>
<tr><td>Cross-sectional averaged pressure</td><td><table><tr><th>Grid type</th><th>Elevation range (z_1 mm)</th></tr><tr><td>MVG</td><td>-104~175; 452~731</td></tr><tr><td>SSG</td><td>176~455</td></tr></table></td><td>-</td></tr>
<tr><td>Mean axial velocity: interior sub-channel averaged</td><td><table><tr><th>Span</th><th>Elevation (mm)</th></tr><tr><td>1a (z_1)</td><td>25, 50, 75, 100, 175, <u>250</u></td></tr><tr><td>2a (z_2)</td><td>25, 50, 75, 100, 175, <u>210</u></td></tr></table></td><td> 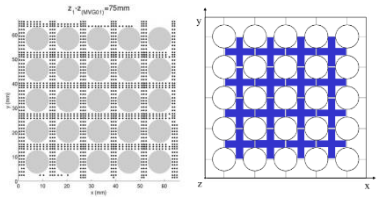 </td></tr>
<tr><td>Mean axial velocity and RMS axial velocity fluctuation</td><td><table><tr><th>Span</th><th>Elevation (mm)</th></tr><tr><td>1a (z_1)</td><td>25, 50, 75, 100, 175, <u>250</u></td></tr><tr><td>1b (z_1)</td><td>304, 379, 514</td></tr><tr><td>2a (z_2)</td><td>25, 50, 75, 100, 175, <u>210</u></td></tr><tr><td>2b (z_2)</td><td>304, 379, 514</td></tr></table></td><td> 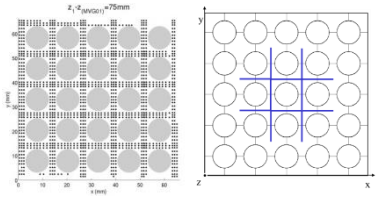 </td></tr>
</table>

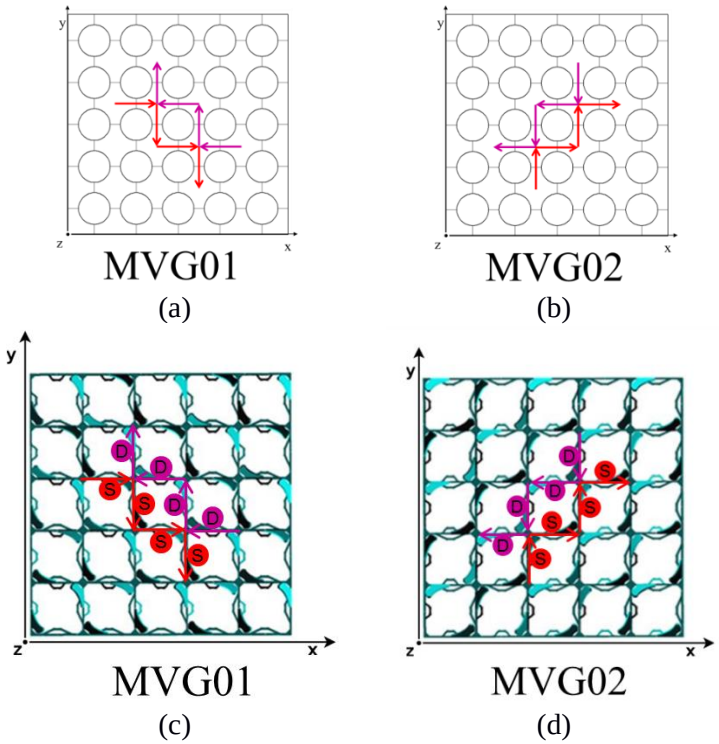

Figure 4 Lateral range spring(red) and dimple(magenta) vector lines adopted for axial velocity comparisons along MVG wake regions (span 1a and span 2a): (a) range MVG01, (b) range MVG02, (c) MANIVEL MVG01 orientation, and (d) MVG02 orientation.

2.3.2 OMEGA-MVG bundle: heated experiment

CFD-code-to-experiment benchmark comparisons for the heated single-phase OMEGA MVG bundle test consist of rod inner-surface temperature, as shown in Table 9 by EPRI [11]. Inner-rod wall circumferential temperature distribution along MVG wake regions for all measured rods (Rod 1-9) was compared. Inner-rod wall temperature distribution averaged at each measured elevation was compared for all measured rods (Rod 1-9).

Table 9 OMEGA MVG bundle: CFD-code-experiment variables; axial and lateral measurement ranges, reprinted with permission EPRI [11].

<table>
<tr><th>Variables</th><th>Axial range</th><th>Lateral range</th></tr>
<tr><td></td><td> 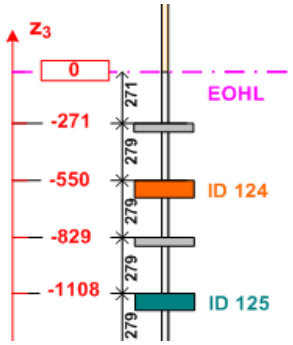
</td><td> 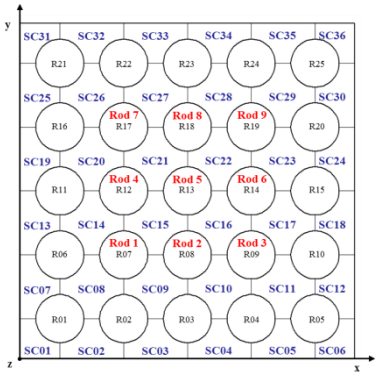
</td></tr>
<tr><td>Circumferential inner-rod wall temperature distribution</td><td rowspan="2"><table><tr><th>Span</th><th>Elevation (z_3 mm)</th></tr><tr><td>MVG02</td><td>-1090, -1060, -1030, -1002,-970, -942, -912, -882, -852</td></tr><tr><td>MVG01</td><td>-530, -500, -470, -440, -410,-380, -350, -320, -290</td></tr></table></td><td>Rods 1, 2, and 5
Azimuthal: $\theta = 0^\circ \sim 360^\circ$
 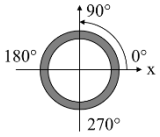
</td></tr>
<tr><td>Axial distribution of elevation averaged rod inner-surface temperature</td><td>Rods 1-9</td></tr>
</table>

3 CFD METHODOLOGIES

CFD codes are used as an analysis tool to practically gain insight into fluid interactions with surfaces defined by appropriate boundary conditions. The appropriate selection of CFD methodologies for a specific study is imperative to the fidelity of the CFD result generated. Computational boundary conditions, mesh parameters, turbulence models, near-wall treatment, and numerical scheme were strategically investigated to balance computation cost and solution accuracy. Mesh size sensitivity studies investigated a typical grid span's global base size, and extruded bare-rod cells' axial length in the support grids' far upstream and downstream wake regions. Approximate relative error and mean axial velocity line profiles were compared between mesh refinements.

3.1 Computational domains and boundary conditions

Table 10 presents the computation domains and boundary conditions adopted for CFD-code-to-experiment benchmark comparisons. The isothermal CFD calculations on the MANIVEL MVG bundle considered the six uppermost support grids spanning $z_1 = -396mm \sim 1271mm$. Heated CFD calculations on the OMEGA MVG bundle considered the complete heated length spanning $z_3 = -3658mm \sim 0mm$. Both isothermal and heated CFD calculations adopted the full 5×5 rod bundle array lateral domain. Heated CFD calculations considered conduction through the rod cladding thickness for all 25 heated rods with conjugate heat transfer modeling. The following flow-to-wall boundary conditions were adopted for isothermal and heated CFD calculations; (i)

uniform mass flow rate inlet, (ii) pressure outlet, and (iii) no-slip on wall surfaces (casing, rods, and support grids). Star-CCM+ interprets the uniform mass flow inlet as a constant velocity condition appropriate for the flow area. Heated CFD calculations adopted the following thermal boundary conditions; (i) uniform inlet temperature; (ii) adiabatic conditions on casing walls, support grids, and rod inner diameter surfaces; (iii) uniform volumetric source for the nine inner and 16 peripheral heated rods, and (iv) mapped interface at the fluid/solid boundary for all 25 heated rods.

Table 10 Computational boundary conditions: MANIVEL MVG and OMEGA MVG bundles.

MVG bundle	Boundary condition	Description
MANIVEL	Axial domain	$z_1 = -396mm \sim 1271mm$ (top six spans)
OMEGA	Axial domain	$z_3 = -3658mm \sim 0mm$ (heated length)
Both	Lateral domain	Fluid: 5×5 (full rod bundle array)
OMEGA	Lateral domain	Rods: all 25 heated rods
Both	Flow	Uniform flow inlet; pressure outlet; no-slip (wall surfaces - casing, rods, support grids)
OMEGA	Thermal: fluid region	Uniform inlet temperature; adiabatic surface (casing walls and support grids)
OMEGA	Thermal: solid rods	Uniform volumetric heat source; adiabatic surface (rod inner diameter surfaces)
OMEGA	Thermal: interfaces	Mapped contact interface between fluid region and solid rods for rod outer diameter surfaces

3.2 Turbulence models with associated near-wall treatment

Table 11 presents examined- isotropic and anisotropic turbulence models, near-wall treatment, and numerical schemes- for isothermal and heated CFD calculations. The two-equation standard k-ε linear eddy viscosity model, abbreviated as LEVM, with transport equations for turbulent kinetic energy and dissipation rate suggested by Jones

and Launder [14] and coefficients from Launder and Sharma [15] served as an isotropic turbulence model. Applying coefficients suggested by Baglietto et al. [16] to the quadratic k-ε turbulence model served as an anisotropic modified quadratic k-ε turbulence model, abbreviated as mQKE. The Reynolds stress transport model with quadratic pressure strain correlation formulated by Speziale et al. [17] was adopted. Stated turbulence models adopted a wall function (high-y+ treatment in the Star-ccm+ code by CD-adapco [18]) for near-wall treatment.

Table 11 RANS CFD methodologies: MANIVEL MVG and OMEGA MVG bundles.

CFD methodology	Description
Turbulence models	Standard k-ε (LEVM); modified quadratic k-ε (mQKE) ; Speziale-Sarkar-Gatski Reynold stress model (SSG-RSM)
Wall treatment	High y+ wall function (law-of-the-wall)
Numerical scheme: temporal	Steady
Numerical scheme: spatial	2^{nd} order upwind

3.3 Mesh

The computational domain was discretized using the Star-CCM+ mesh generation algorithm to construct an unstructured trimmed mesh for the fluid region, and prismatic type mesh for the solid rods. A hexahedral template grid is first applied to the fluid domain. Then the meshing algorithm trims or cuts the hexahedral template to accommodate geometric surfaces with prism layers extruded from the solid boundary towards the fluid region for a more accurate near-wall value, called prism layers by CD-

adapco [18]. The mesh within the solid rods consists of prism layers. The adopted mesh generation process, mesh type, and mesh configuration have been used by Conner et al. [7] for similar CFD methodology, and validation applications regarding 5×5 rod bundle with support grids examined through a round robin benchmark by EPRI [11]. Table 12 presents adopted meshing parameters and values for isothermal and heated CFD calculations.

Table 12 Meshing parameters: MANIVEL MVG and OMEGA MVG bundles

MVG bundle	Domain	Feature	Description
Both	Fluid	Type	Trim mesh with extruded near-wall prism layers
MANIVEL	Fluid	Notes	85.11M total cells; 23.8M cells/MVG span ; 9.4M cells/SSG span
OMEGA	Fluid	Notes	214.43M total cells; 24.1M cells/MVG span ; 9.9M cells/SSG span
Both	Fluid	Prism layers	MVGs and SSGs: 1
MANIVEL	Fluid		Rods and casing walls: 2
OMEGA	Fluid		Rods and casing walls: 5
OMEGA	Rods	Type	Thin mesher: 6 prism layers
OMEGA	Rods	Notes	63.11M total cells; 7.7M cells/MVG span ; 2.5M cells/SSG span

3.3.1 Mesh configuration

Due to the size and complexity of the MANIVEL MVG and OMEGA MVG bundles, computation domain simplifications were adopted to reduce computational resources for large CFD calculations, while adequately resolving the following detailed geometric features; MVGs, SSGs, and near-wall regions. The fluid core region of a grid and adjacent bare-rod regions consist of uniform hexa and trimmed hexa cells with sufficient refinement near all walls, while the solid rods consist of prism layers. MVG and SSG

span types were sub-divided into three characteristic regions: (i) far upstream and downstream extruded bare-rod regions, (ii) near upstream and downstream refined regions, and (iii) grid region, as shown in Figure 5. Regions (i) and (ii) have the same lateral grid size, but grid points in region (i) were axially extruded to reduce the total number of grid points. Region (iii) for SSG spans incorporates high refinement near all wall and core regions approximately one rod diameter upstream of the SSG bottom, within the SSG, and approximately two rod diameters upstream of the SSG top, as well as elongated grid point upstream and downstream of stated regions, as shown in Figure 5 (a). Region (iii) for MVG spans incorporates high refinement near all walls and core regions approximately 1 rod diameter upstream of the MVG bottom, within the MVG, and approximately 6 rod diameters upstream of the MVG top, with elongated grid point upstream and downstream of stated regions, as shown in Figure 5 (b). Individual MVG and SSG spans were combined to form the MANIVEL MVG and OMEGA MVG bundles.

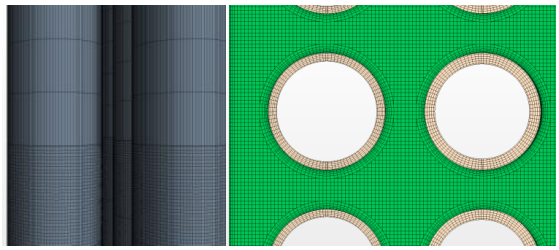

(i) and (ii)

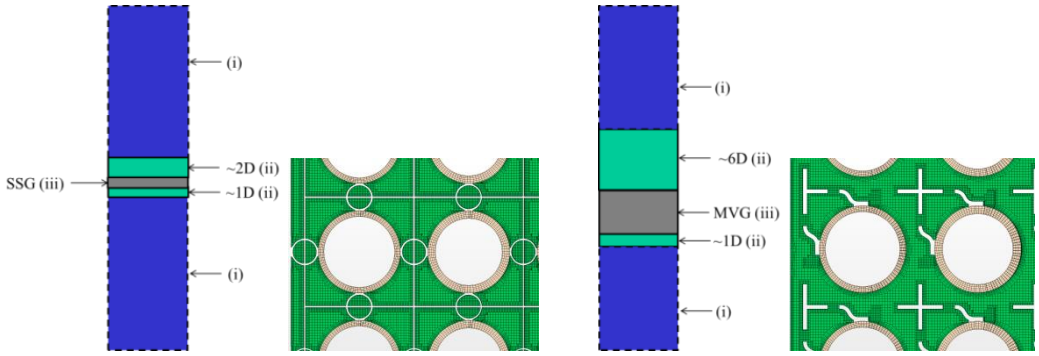

(a) (b)

Figure 5 Mesh configurations for (a) SSG span and (b) MVG span.

3.3.2 Mesh size sensitivity studies

Adopting a sufficiently fine mesh for stated mesh configurations is required prior to making CFD-code-to-experiment comparisons. Mesh refinements were modified with respect to selected characteristic support grid span region [Figure 5] while keeping other CFD methodological considerations the same. Each mesh size sensitivity case adopted the stated MANIVEL MVG bundle computational domain, isothermal operating conditions [Table 4], and standard k-ε turbulence model with high-y+ wall function.

Mesh size sensitivity studies examined extruded axial mesh size for region (i) [Figure 5], and global base mesh size for all regions [Figure 5 (a) and (b)], as shown in Table 13 and Table 14. Table 13 (a) describes the axial mesh refinement of extruded bare-rod cells within region (i), referred to as A# and axial size. Table 13 (b) describes the global base refinement for all regions (except extruded bare-rod cells within region (i)), referred to as B# and base size. The number of extruded prism layers from each rod and casing wall boundaries is listed in Table 14. Prism layers were not extruded from support grid walls. The near-wall regions adjacent to support grid walls are approximately half the listed base size. The volume ratio between axially adjacent cells at the axial mesh height discontinuity [Figure 5 (i)] is described for each mesh refinement, as shown in Table 14.

Table 13 Mesh sensitivity size labels; (a) axial mesh length of extruded bare-rod cells within region (i) [axial], and (b) global base size for all regions [global].

(a)

	Axial Size
Label	**(mm)**
A3	9.50
A2	4.75
A1	2.38

(b)

	Base Size
Label	**(mm)**
B3	0.60
B2	0.30
B1	0.23

Table 14 Mesh sensitivity test matrix: (a) axial, and (b) global.

(a)

Mesh Label	Prism Layers	Volume Ratio	Total Cells (million)
A3-B2	3	30.45	82.65
A2-B2	2	15.95	86.84
A1-B2	2	7.97	95.68

(b)

Mesh Label	Prism Layers	Volume Ratio	Total Cells (million)
A2-B3	3	7.96	20.34
A2-B2	2	15.95	86.84
A2-B1	2	20.80	159.30

Mean axial velocity at point locations along stated vector line profiles at various axial and lateral ranges [Table 8] were compared between stated mesh refinements to identify

a sufficiently fine mesh for CFD-code-to-experiment benchmark comparisons. In order to compare mean axial velocity point values between significantly different mesh refinements, the extracted point value from each mesh refinement must have the same centroid within the spatial domain. If the centroids between mesh refinements are slightly different, then the extracted values will not correspond and institute an additional source of error. Accordingly, the solution from a finer mesh was mapped (least squares interpolation) onto the coarse mesh, so all extracted point centroids' correspond with the coarse mesh centroid. This method guaranteed that various mesh refinements' mean axial velocity point values shared the same centroid location.

4 RESULTS AND DISCUSSION

This section presents results from mesh size sensitivity studies and CFD-code-to-experiment benchmark comparisons. Axial and global mesh size sensitivity studies compared mean axial velocity line profiles and approximate relative error between mesh refinements. As a result, CFD-calculations adopted a sufficiently fine mesh for CFD-code-to-experiment benchmark comparisons. Dimensionless wall distance (y+) was examined on no-slip boundaries for all CFD calculations adopted for CFD-code-to-experiment benchmark comparisons.

CFD-code-to-experiment benchmark comparisons were examined for isothermal and heated test case on the MANIVEL MVG and OMEGA MVG rod bundles, respectively. Isothermal benchmark comparisons include: (i) SSG and MVG grid-span pressure loss ratios; flow variables include (ii) mean axial velocity distribution along MVG wake region, and (iii) mean axial velocity and RMS axial velocity fluctuation vector line profiles along MVG and SSG wake regions. Thermal benchmark comparisons consisted of inner-diameter surface temperature distributions along MVG wake regions for Rods 1-9 with respect to the axial and azimuthal directions.

4.1 Mesh size sensitivity studies

Mean axial velocity (v) approximate relative errors [equations 1, 2, and 3], and mean axial velocity profiles were examined between axial and global mesh size perturbations, with respect to mesh refinement A2-B2.

$$e_a^{A3A1} = \frac{1}{N}\sum_{i=1}^{N}\left|\frac{v_{A1B2_i} - v_{A3B2_i}}{v_{A1B2_i}}\right|; e_a^{B3B1} = \frac{1}{N}\sum_{i=1}^{N}\left|\frac{v_{A2B1_i} - v_{A2B3_i}}{v_{A2B1_i}}\right| \quad (1)$$

$$e_a^{A3A2} = \frac{1}{N}\sum_{i=1}^{N}\left|\frac{v_{A2B2_i} - v_{A3B2_i}}{v_{A2B2_i}}\right|; e_a^{B3B2} = \frac{1}{N}\sum_{i=1}^{N}\left|\frac{v_{A2B2_i} - v_{A2B3_i}}{v_{A2B2_i}}\right| \quad (2)$$

$$e_a^{A2A1} = \frac{1}{N}\sum_{i=1}^{N}\left|\frac{v_{A2B1_i} - v_{A2B2_i}}{v_{A2B1_i}}\right|; e_a^{B2B1} = \frac{1}{N}\sum_{i=1}^{N}\left|\frac{v_{A2B1_i} - v_{A2B2_i}}{v_{A2B1_i}}\right| \quad (3)$$

Axial mesh size perturbations indicated the following approximate relative percent errors; from A3-B2 to A1-B2 of 0.403%; from A3-B2 to A2-B2 of 0.346%; from A2-B2 to A1-B2 of 0.089%, as shown in Table 15(a). Global base mesh size perturbations indicate the following approximate relative percent errors; from A2-B3 to A2-B1 of 1.632%; from A2-B3 to A2-B2 of 1.283%; from A2-B2 to A2-B1 of 0.741%, as shown in Table 15 (b).

Table 15 Mean axial point velocity averaged approximate relative difference for Spans 1 and 2; (a) axial, and (b) global.

(a)

e_a^{A3A1}(%)	0.403
e_a^{A3A2} (%)	0.346
e_a^{A2A1}(%)	0.089

(b)

e_a^{B3B1} (%)	1.632
e_a^{B3B2} (%)	1.283
e_a^{B2B1} (%)	0.741

Mean axial velocity profiles for axial mesh size refinements conveyed sensitivity to refinements in the axial length of extruded bare-rod cells for both MVG and SSG near

(25mm) and intermediate (75mm) wake regions, as shown in Figure 6 (a) and (b), respectively. These sensitivity regions coincide with the first measured axial locations downstream of the mesh discontinuity, as shown in Figure 5. Comparisons for all other wake regions show negligible sensitivity between examined axial mesh refinements. Similarly, global base size refinements observed sensitivity in both MVG and SSG near wake regions (25mm), as shown in Figure 6 (c) and (d), respectively. Comparisons at all other wake regions show comparable sensitivity between examined global mesh refinements.

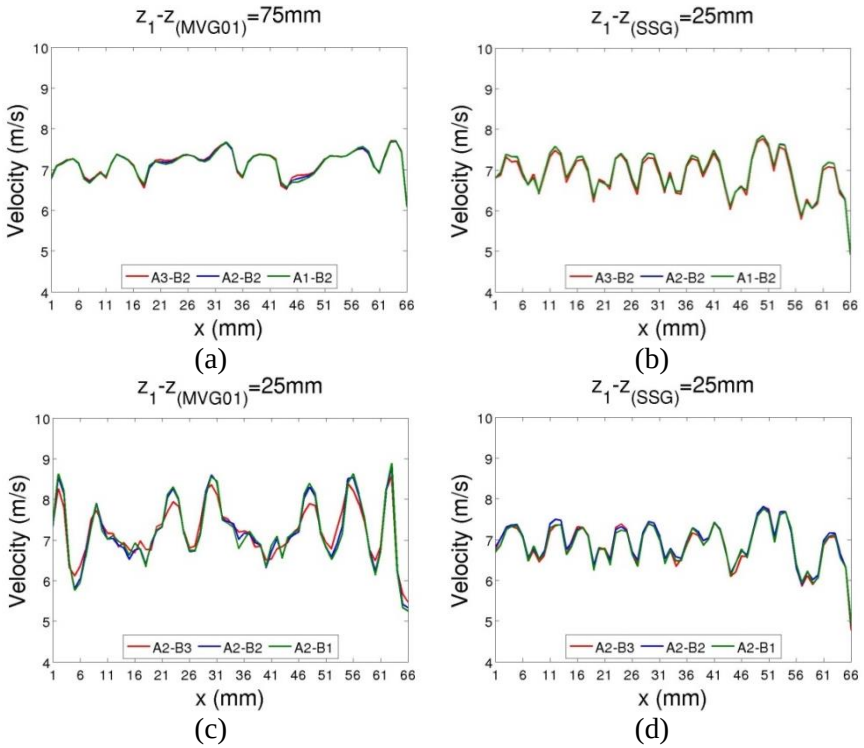

Figure 6 mean axial velocities comparisons along line 3 at selected axial heights in span 1; (a) axial MVG, (b) axial SSG, (c) global MVG, and (d) global SSG.

Approximate relative errors and mean axial velocity profiles between examined axial mesh refinements indicate only minor sensitivity to mean axial velocity values, even though the interfacial volume ration increases from ~8 to ~30 [Table 13]. Similarly, A2-B3 to A2-B2 global base sizes indicate considerable sensitivity to mean axial velocity values, whereas stated values show less sensitivity between A2-B2 to A2-B1 refinements. CFD-to-experiment validation comparisons adopted 4.75mm and 0.30 mm for the axial length of extruded bare-rod cells and global base mesh size, respectively.

4.2 Dimensionless wall distance

The percent distribution of y+ values and average y+ value for no-slip boundaries were examined for isothermal and heated CFD-code-to-experiment benchmark comparisons, as shown in Table 16. The following no-slip boundaries (i) rod and casing walls, (ii) MVGs, and (iii) SSGs have y+ values ranging from 30 to150 for approximately (i) 92% to 98%, (ii) 86% to 96%, and (iii) 21% to 87% of all adjacent near-wall cells, respectively. Furthermore, the average y+ value for stated no-slip boundaries range between; (i) ~49 to ~60, (ii) ~39 to ~102, and (iii) ~25 to ~68, respectively.

Table 16 Percent distribution of y+ values ranging from 30-150 (average y+ value)

No-slip BC	LEVM [% (avg)]		mQKE [% (avg)]		SSG-RSM [% (avg)]	
	MANIVEL	OMEGA	MANIVEL	OMEGA	MANIVEL	OMEGA
Rods	92.9(~55)	98.0(~62)	92.7(~54)	98.0(~62)	92.0(~55)	98.0(~62)
Casing walls	92.8(~50)	98.0(~57)	92.6(~49)	98.3(~60)	93.2(~50)	98.3(~57)
MVGs	96.4(~44)	94.8(~102)	93.0(~40)	94.9(~90)	85.7(~39)	94.5(~86)
SSGs	71.1(~31)	86.8(~68)	49.7(~29)	86.2(~60)	20.7(~25)	81.2(~59)

4.3 Grid span pressure loss

To ensure a consistent pressure loss comparison between CFD and experimental results under different thermal hydraulic conditions, a one-span pressure loss coefficient (P_{loss}) defined as $P_{loss} = \Delta P_{1span}/(\frac{1}{2}\rho {V_0}^2)$ where ΔP_{1span} is measured or calculated one-span pressure loss; ρ is density, and V_0 is bulk velocity. The one-span pressure loss ratio for MVG and SSG spans were normalized with respect to the corresponding experimental pressure loss, as shown in Figure 7. Examined isotropic and anisotropic turbulence models- LEVM, mQKE, and SSG-RSM - over-predict the pressure loss ratio for the MVG span by 4.7%, 0.8%, and 0.6%, respectively. Similarly for the SSG span, LEVM over-predict the pressure loss ratio by 0.1%, while mQKE and SSG-RSM under-predicted by 2.8% and 0.7%, respectively. SSG-RSM and mQKE turbulence models exhibits lower pressure losses for both MVG and SSG spans compared to the LEVM model. This difference is due to the lower pressure loss across the grid, as opposed to the pressure gradient difference in the far wake region, as shown in Figure 7 (a) and (b).

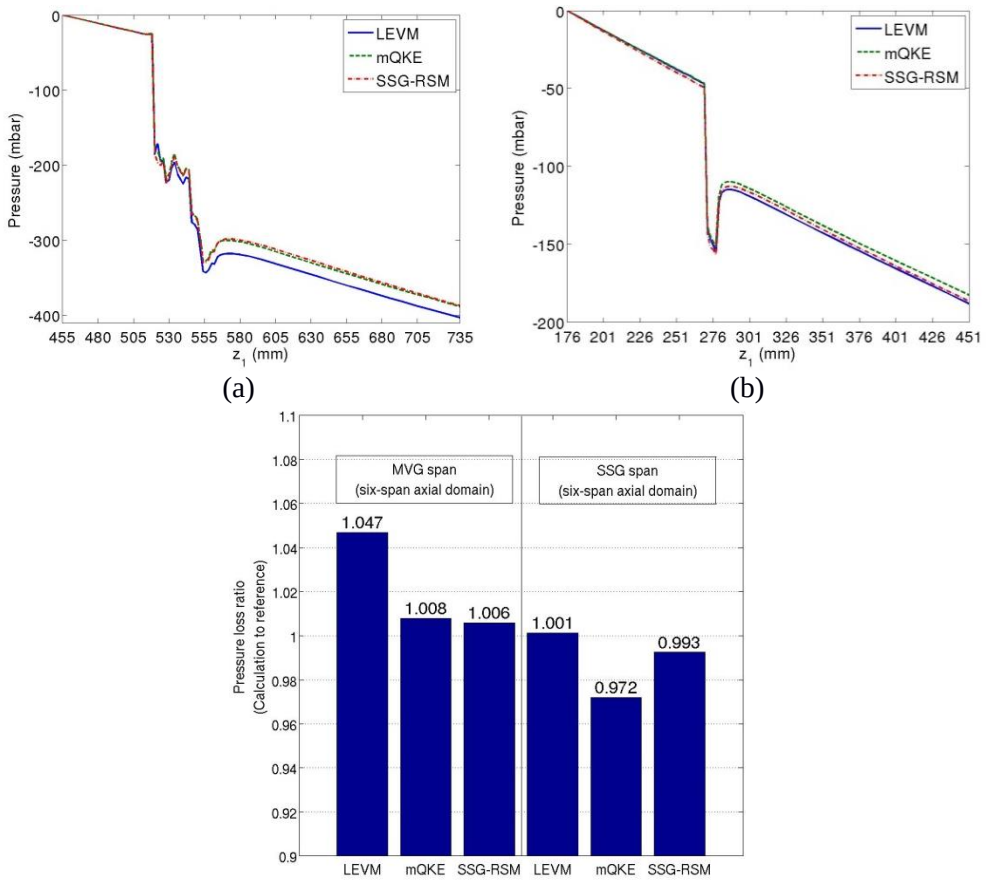

Figure 7 (a) MVG span axial pressure distribution, (b) SSG span axial pressure distribution, and (c) MVG and SSG one-span pressure loss coefficients.

4.4 Flow variables

Two key challenges significant to the heated MVG rod bundle problem include; (i) accurately predicting circumferential location of hot spots, and (ii) the magnitude of hot spots on rod wall surfaces. Spatial periodicity-related flow behaviors between two MVG spans, and global flow reorientation in the MVG wake region may impact the specific circumferential location and magnitude of hot spots on rod wall surfaces. Even though the isothermal experiment on the MANIVEL MVG bundle does not directly address these challenges, insight can be extracted from flow variables by analyzing the following

characteristics; (i) bulk axial flow distribution along the MVG wake region, and (ii) spring and dimple effect on local axial flow structures along MVG and SSG wake regions.

4.4.1 Sub-channel averaged mean axial velocity along the MVG span

CFD-code-to-experiment comparisons for sub-channel averaged mean axial velocity values were examined to show bulk axial velocity distribution as the flow progressed along the MVG wake region, as shown in Figure 8. The top column of Figure 8 presents lateral domain decomposition for sub-channel averaged mean axial velocity comparisons. The purple arrow indicates orientation of mixing vanes. Also, the solid and dashed lines represent MVG01 and MVG02, respectively. Each MVG span was decomposed into two sub-channel domain categories consisting of; (i) interior without center sub-channels, and (ii) center sub-channels, as shown in the right and left column of Figure 8, respectively. Each domain category was also decomposed into two directional categories; (i) orientation along the mixing vanes, and (ii) orientation 45° about the z-axis of the mixing vanes (non-vane orientation), as highlighted in Figure 8 by magenta and yellow sub-channels, respectively. Global cross-flow reorientation in the counter clockwise direction with respect to original mixing vane orientation in MVG span wake region is qualitatively captured by the steady SSG-RSM turbulence model.

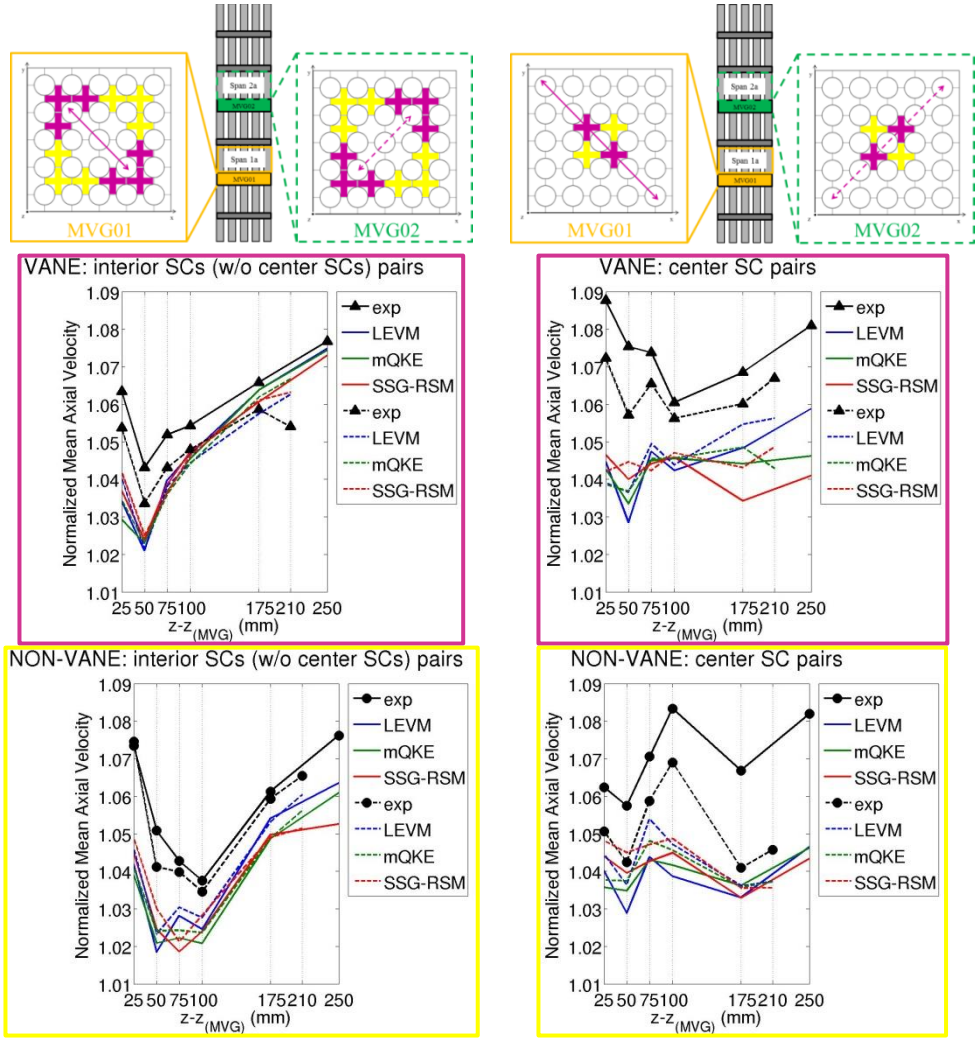

Figure 8 axial flow distribution along MVG wake regions

4.4.2 Spring and dimple mean axial velocity vector line profiles along the MVG span

This section compares measured and CFD-calculated normalized mean axial velocity profiles along spring and dimple rod-to-gap center vector lines in the MVG wake regions of Span 1a and Span 2a.

Spatial periodicity-related flow behaviors between two MVG spans was examined for measured and calculated mean axial velocity values, as shown in Figure 9 (LEVM and mQKE not shown). Solid lines represent span 1a profiles and dashed lines represent span 2a profiles. Measured spring and dimple profiles have similar flow patterns between two MVG spans, but do not show periodicity in magnitude. This difference may be caused by inlet flow condition, or measured location between the two spans. In contrast, calculated all steady RANS (LEVM, mQKE, SSG-RSM) calculations exhibit spatial periodicity-related behavior between two MVG spans regarding both flow pattern and magnitude, as shown in Figure 9. Further, EPRI [11] describes similar spatial periodicity-related behavior when adopting similar CFD methodological factors; steady RANS turbulence models with associate high-y+ wall function, sufficiently fine trim type mesh, and with additional upstream MVG and SSG spans.

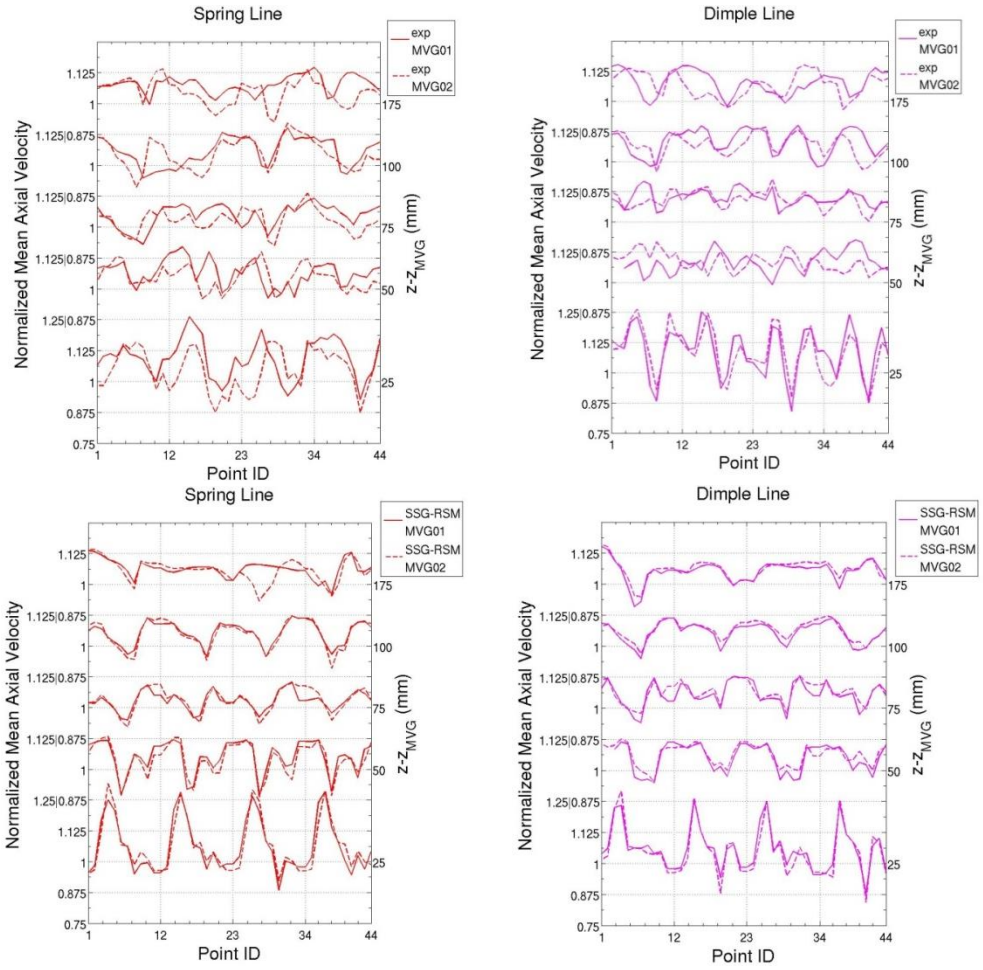

Figure 9 Mean axial velocity comparison between MVG01 Span 1a and MVG02 Span 2a for measured and calculated (SSG-RSM) values.

CFD-code-to-experiment spring and dimple mean axial velocity benchmark comparisons were examined, as shown in Figure 10. The overall distribution of mean axial velocity along spring and dimple lines are comparable, but localized flow structure shows distinguishable discrepancies between CFD calculations and experimental results in the near and far downstream regions. The intermediate downstream region shows more comparable localized flow structure between CFD calculations and experimental results.

LEVM and mQKE turbulence models show very similar results at all elevations for the MVG span.

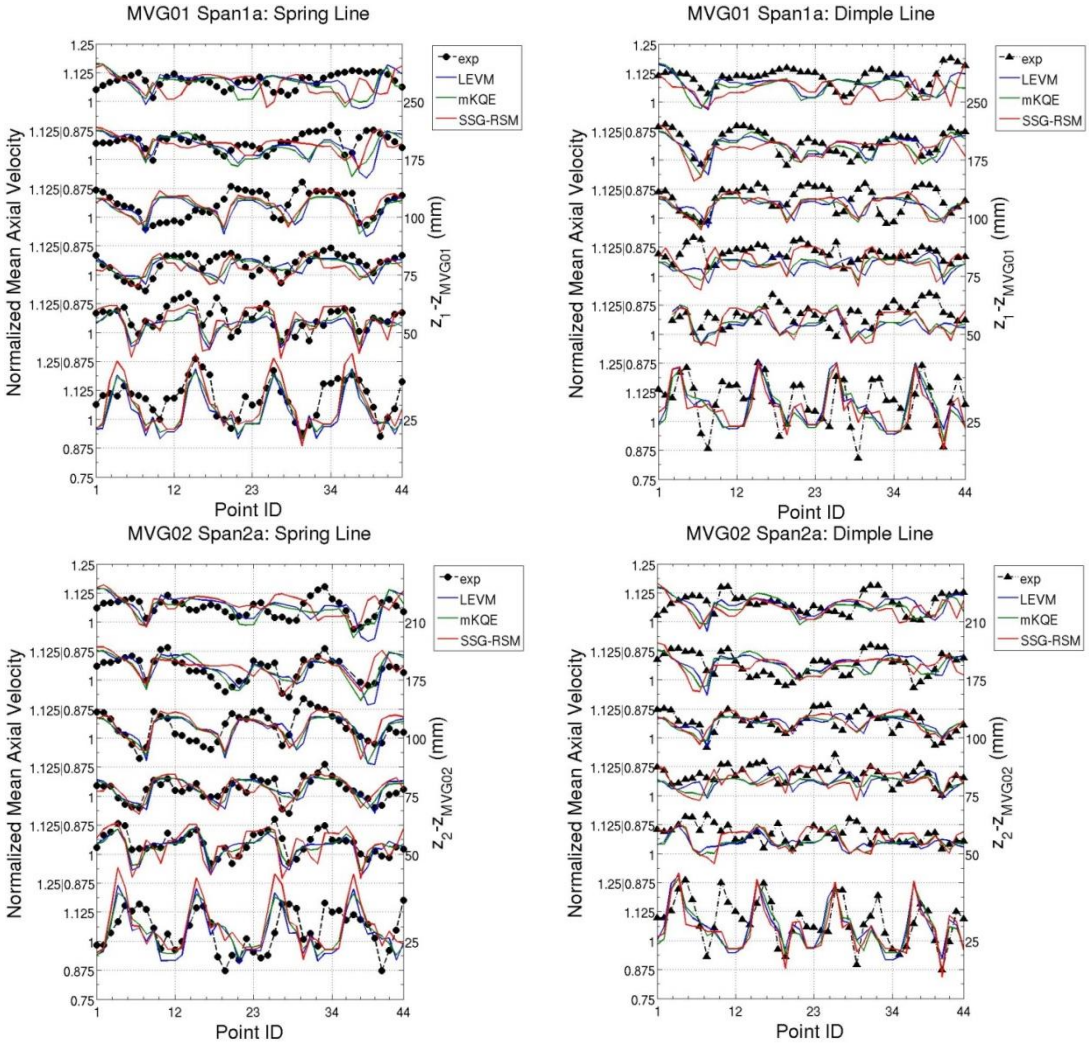

Figure 10 Normalized mean axial velocity along spring and dimple vector lines at various elevations in span 1a and span 2a.

4.4.3 Spring and dimple mean axial velocity vector line profiles along the SSG span

Spring and dimple vector lines were adopted for mean axial velocity CFD-code-to-experiment comparisons at various elevations within the core region of span 1b and 2b, as shown in Figure 11. Comparisons show good agreement between examined CFD calculations and experimental results in the near, intermediate, and far downstream regions. At $z_1 - z_{(MVG)} = 514mm$, the anisotropic turbulence models, mQKE and SSG-RSM, have better agreement with measured values compared to the isotropic LEVM turbulence model. This may suggest the anisotropic turbulence models recognize the presence of secondary flow structures [circled in Figure 12(b) and (c)] typically found in bare-rod bundles, described by Vonka [19]; while the isotropic turbulence model does not, as shown in Figure 12 (a). The presence of secondary flow structures in the far wake region of the SSG (Span 1b) indicates a significant reduction in cross-flow generated by the mixing vanes (span 1a).

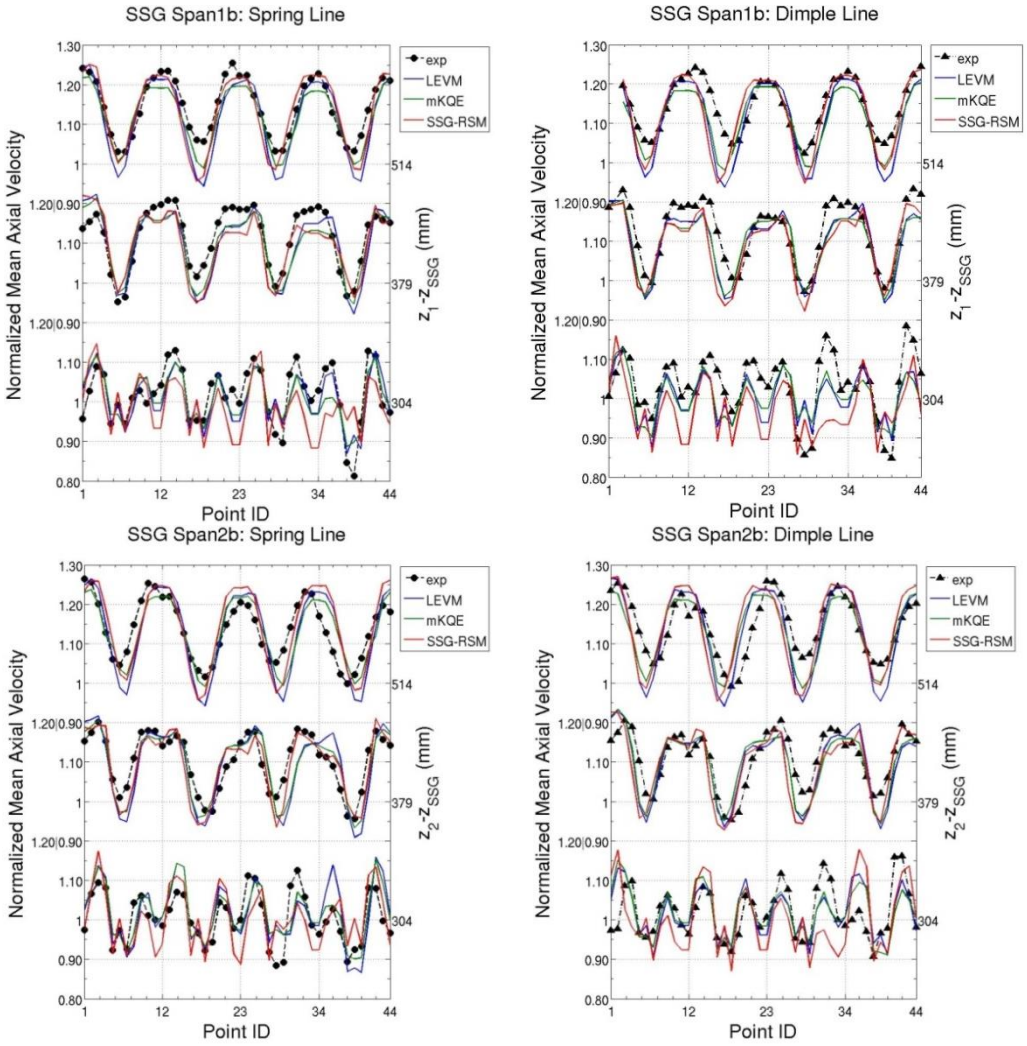

Figure 11 Normalized mean axial velocity along spring and dimple vector lines at various elevations in span 1b and span 2b.

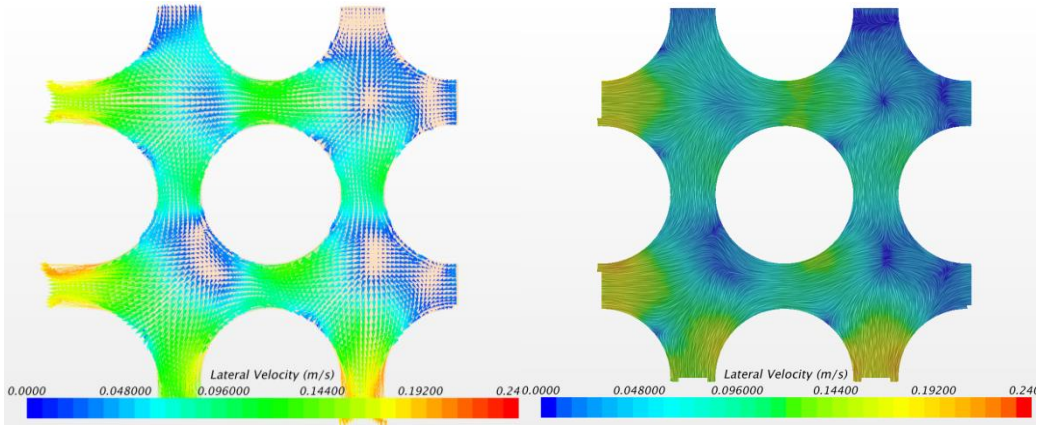

(a)

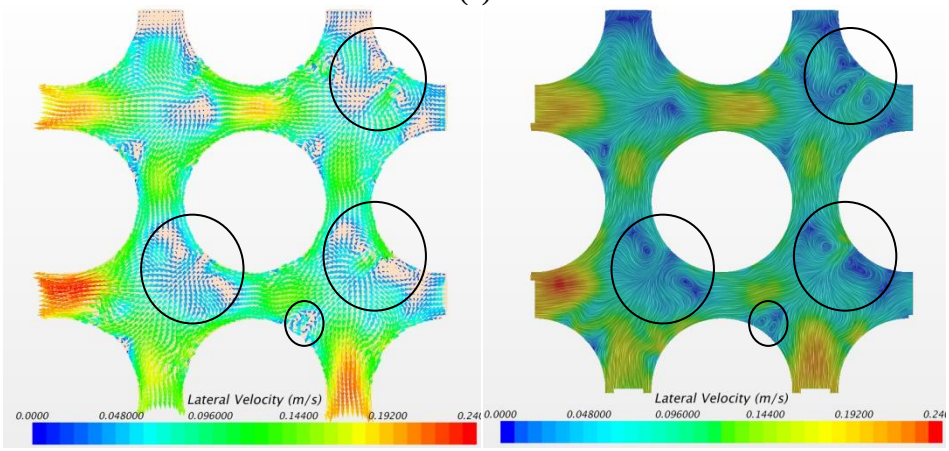

(b)

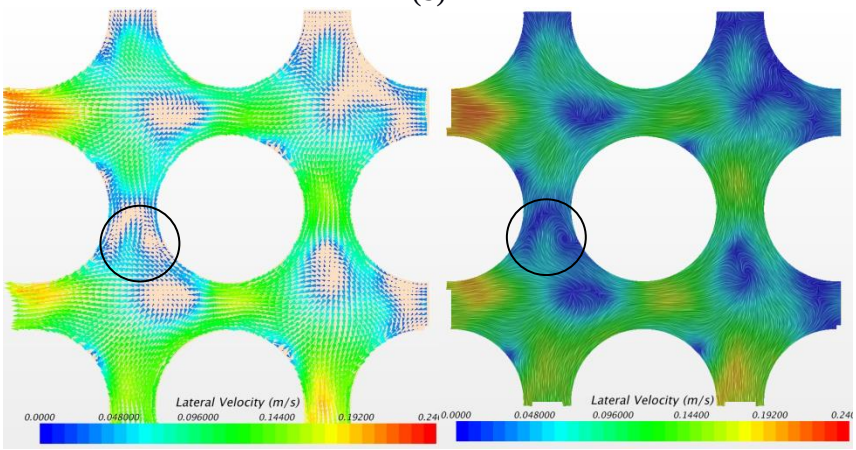

(c)

Figure 12 Mean lateral velocity field at z-$z_{(MVG)}$=514mm for sub-channels surrounding Rod 5 (SC15, SC16, SC21, and SC22); (a) LEVM, (b) mQKE, and (c) SSG-RSM.

4.4.4 Spring and dimple RMS axial velocity fluctuation vector line profiles along the MVG span

RMS axial velocity fluctuation spring and dimple vector line profiles were compared along the wake of the MVG span1a and span 2a, as shown in Figure 13. CFD-code-to-experiment comparisons show good agreement in the MVG's near wake region ($z - z_{(MVG01)} = 25mm \; and \; 50mm$), but CFD calculations noticeably under-predict RMS axial velocity fluctuation in the MVG's intermediate and far wake regions.

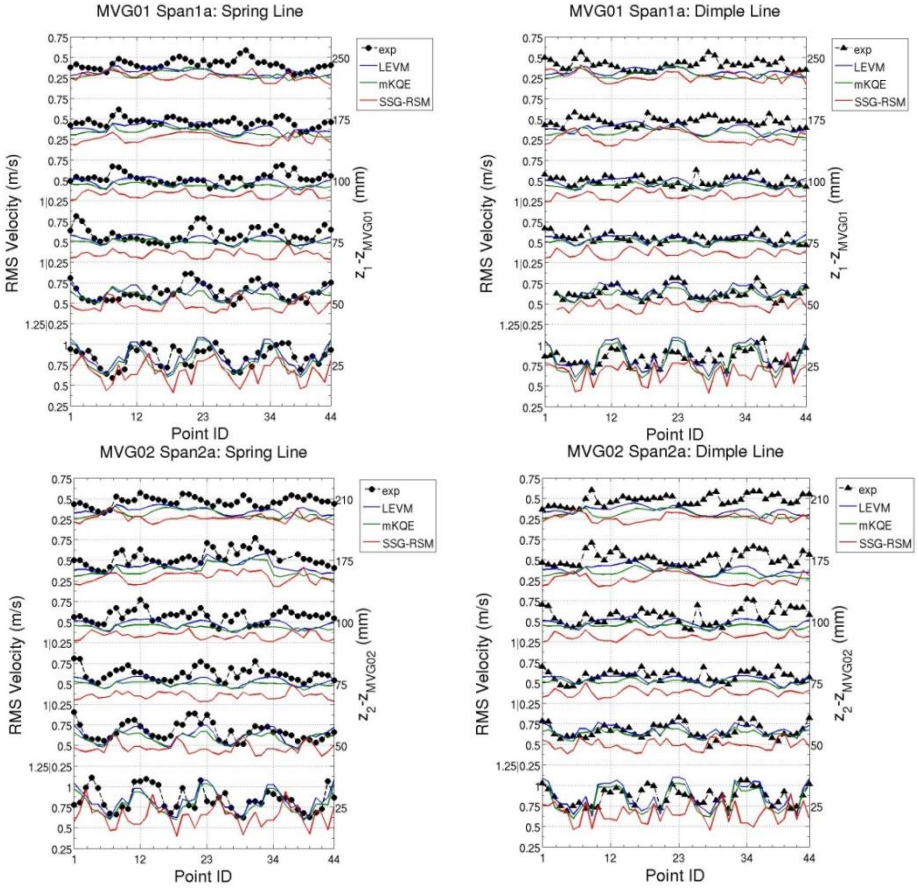

Figure 13 RMS axial velocity fluctuation comparison along spring and dimple vector lines at various span 1a and 2a elevations.

4.4.5 Spring and dimple RMS axial velocity fluctuation vector line profiles along the SSG span

RMS axial velocity fluctuation spring and dimple vector line profiles were compared along the wake of the SSG span1b and span 2b All SSG wake regions under-predict RMS axial velocity fluctuation. The under-predicted trend is similar to that of the MVG span, but more pronounced within the SSG span, as shown in Figure 14.

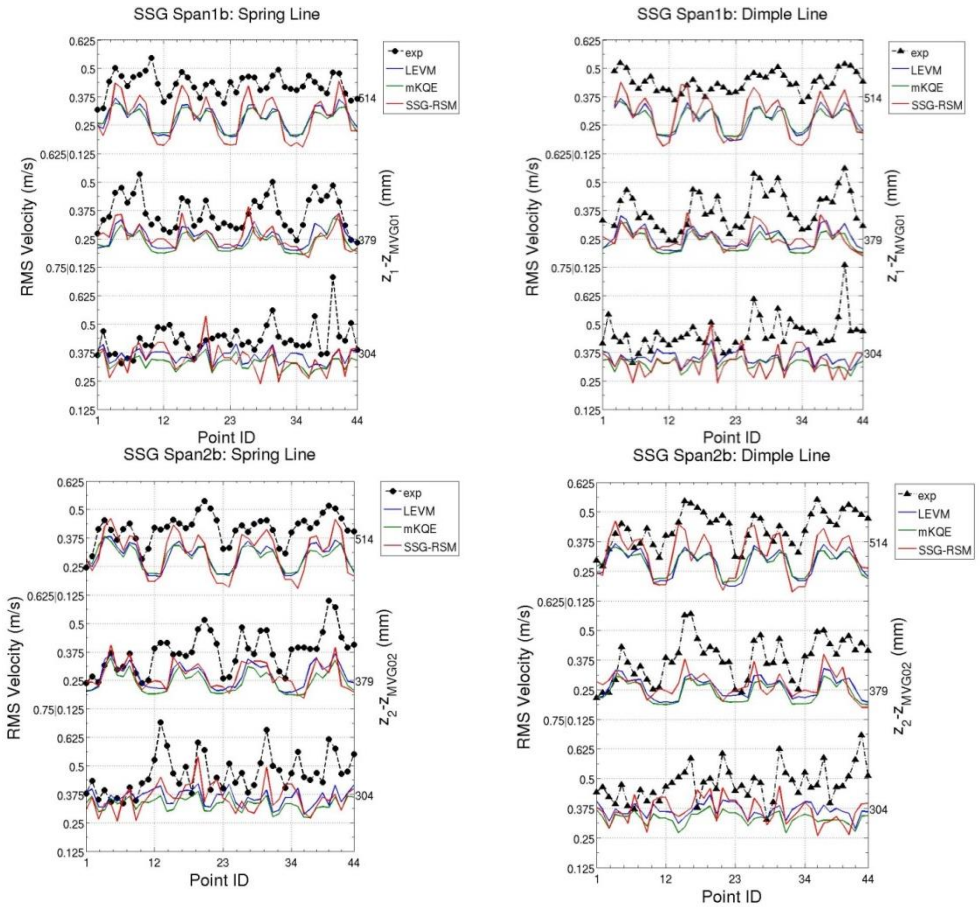

Figure 14 RMS axial velocity fluctuation comparison along spring and dimple vector lines at various span 1b and 2b elevations.

4.4.6 Axial evolution of secondary flow intensity (code-to-code comparison)

Cross-flow in terms of secondary flow intensity was examined as the flow progresses along the MVG and SSG wake regions by averaging secondary flow intensity for interior sub-channel. Secondary flow intensity (FI_{2nd}) is defined as, $FI_{2nd} = \frac{1}{A}\int \frac{\sqrt{\bar{u}_x^2+\bar{u}_y^2}}{\bar{u}_{z,bulk}} dA$, where A is the sub-channel area. Secondary flow intensity exponentially decreased along the downstream MVG wake region. Secondary flow intensity 15mm and 270mm downstream of the top of the grid strap of OMEGA MVG01 is; (i) 0.298 and 0.081 for LEVM, (ii) 0.311 and 0.075 for mQKE, and (iii) 0.334 and 0.109 SSG-RSM, respectively, as shown in Figure 15. Upon passing the SSG (271mm to 279mm), secondary flow intensity abruptly drops (between 265mm and 285mm). Near the inlet of the downstream MVG (SSG far wake region), the secondary flow intensity is 0.012, 0.013, and 0.019 for LEVM, mQKE, and SSG-RSM, respectively.

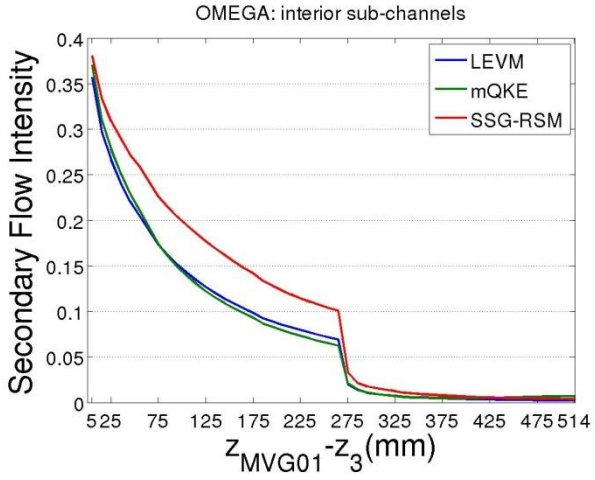

Figure 15 Secondary flow intensity averaged over interior sub-channels at various elevations along OMEGA MVG01 and SSG spans.

4.5 Thermal variables: rod inner-surface temperature

Rod inner-surface temperature was examined for thermal CFD-code-to-experiment benchmark comparisons regarding the heated case (OMEGA MVG bundle). Three types of rod inner-surface temperature distributions were examined; (i) axial distribution of elevation averaged temperature for all and selected inner rods (Rods 1-9), (ii) axial distribution of elevation averaged temperature for selected (Rods 1, 3, 5, 7, and 9) and individual inner rods, (iii) and axial/azimuthal distributions of circumferentially averaged temperature for individual inner rods. Distributions (i) and (ii) adopted the average circumferential rod inner-surface temperature value with respect to rod(s) and elevation. As previously stated, the SSG functions to prevent the rod bundle from vibrating during the experiment, and is not present in a PWR core. Accordingly, selected temperature distribution (ii) and (iii) were only examined along MVG spans.

4.5.1 Axial distribution of elevation averaged temperature along axial range for Rods 1-9

Figure 16 presents measured and calculated elevation averaged temperature for all inner rods. The following qualitative elevation averaged temperature characteristics were observed along the measured axial range: (i) sharp decrease across the MVG extending into the near MVG's near wake region, (ii) gradual increase along the intermediate and far MVG wake regions, (iii) stagnation or slight decrease across the SSG, and (iv) gradual increase along the SSG wake region.

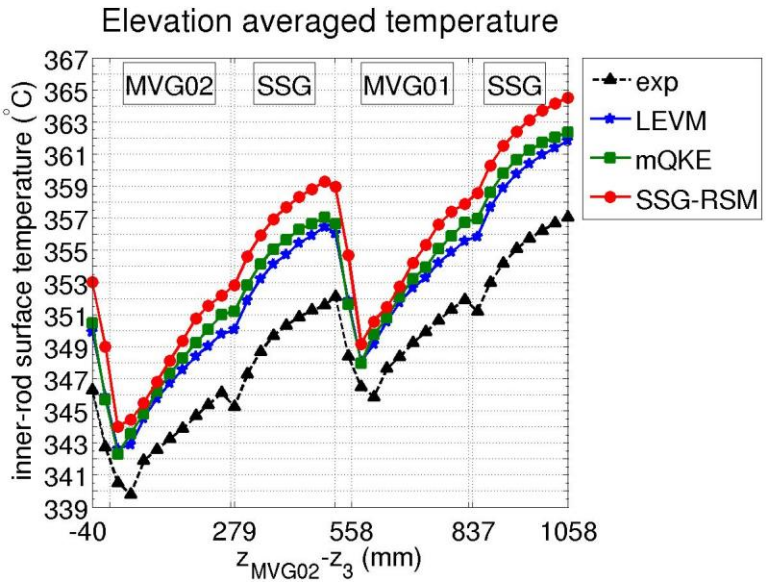

Figure 16 Axial distribution of elevation averaged rod inner-surface temperature along the axial measurement range (MVG02, SSG, MVG01, SSG).

For all examined axial elevations, the CFD calculations overestimate rod inner-surface temperature compared to measured values. This systematic overestimation of temperature along the axial range may be enhanced by the SSG, as shown Table 17. Measured values indicated decreasing temperature across SSG spans of -0.9°C and -0.7°C. However, calculated temperature differences across SSGs increased by 0.3°C, 0.2°, and 0.6°C to 0.7°C for LEVM, mQKE, and SSG-RSM, respectively.

Table 17 Elevation averaged rod inner-surface temperature difference across examined SSGs.

SSG span: rod inner-surface temperature difference (°C)				
axial range (mm)	**exp**	**LEVM**	**mQKE**	**SSG-RSM**
258.5 to 288.0	-0.9	0.3	0.2	0.6
819.5 to 848.8	-0.7	0.3	0.2	0.7

4.5.2 Axial distribution of elevation averaged temperature along MVG span for Rods 1-9

Measured and calculated changes in elevation averaged temperature at near (~19mm) and far (~260mm) MVG wake regions with a reference temperature taken just upstream of the MVG have the following values; (i) ~-5.7°C and ~-0.19 °C for exp, (ii) ~-7.7°C and ~-0.31°C for LEVM, (iii), ~-8.4°C and ~+0.30°C for mQKE, and (iv) ~9.5°C and ~-0.97°C for SSG-RSM, respectively. Examined CFD-calculations over-predicted temperature decrease in the near wake region may be related to cross flow strength in the MVG near wake region, as described in section 4.4.6. Comparing secondary flow intensity for examined turbulence models at near and far wake elevations suggests cross flow strength and elevation averaged temperature rise along the MVG wake regions, suggesting larger secondary flow intensity corresponds to larger heat removal from the rods, thus lower rod temperature, as shown in Figure 15 and Figure 17(b).

Measure temperature values indicate three distinct tends along the MVG wake region; (i) monotonically decreasing along near weak region (until ~50mm), (ii) increases between ~50mm and ~80mm, and (iii) linearly increases with reduced slope between ~80mm and ~260mm, as shown in Figure 17. In contrast, CFD calculations only predict decreasing rod temperature until ~20mm. Temperature profiles then increase in a qualitative linear fashion along the remaining MVG wake region. The temperature profile's slope reduces between ~200mm and ~260mm for SSG-RSM along both MVG spans, as shown in Figure 17.

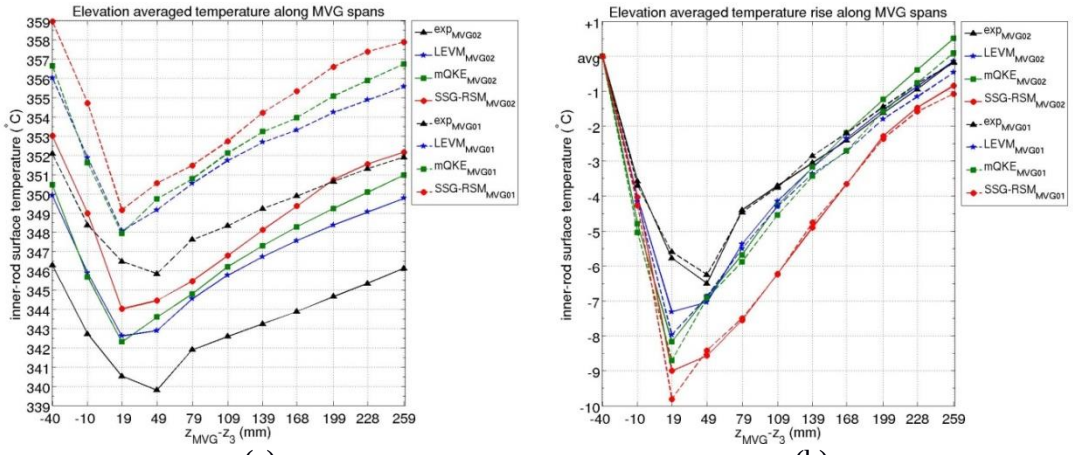

(a) (b)

Figure 17 Axial distribution of elevation averaged rod wall inner-surface- (a) temperature, and (b) temperature rise along MVG02 (solid) and MVG01 (dashed) spans

4.5.3 Axial and azimuthal distributions of elevation averaged temperature for Rods 1, and 5 along MVG02 wake region

Axial and azimuthal distributions of circumferentially averaged rod inner-surface temperature profiles are compared between measured and CFD calculated values along MVG02 wake region for Rods 1, 2, and 5, as shown in the top and bottom columns of Figure 18, respectively.

CFD calculated circumferentially averaged rod inner-surface temperature agree for the following inner rods for the specified ranges with measured values along MVG02 wake regions; Rod 1 [+0.9°C to +5.4°C], Rod 2 [+2.2°C to +5.5°C], and Rod 5 [+1.2°C to +8.8°C], as shown in the top column of Figure 18.

The bottom column of Figure 18 presents the axial and azimuthal distributions of rod inner-surface temperature. The maxima and minima temperature difference (with respect to the elevation average value for each data source) between CFD calculated and measured values for Rods 1 2, and 5 along MVG02 wake region fall within the following ranges; Rod 1 maxima [+1.72°C to +7.15°C] and minima [-8.89°C to -0.43°C]; Rod 2 maxima [+1.92°C to +5.48°C] and minima [-4.71°C to -1.69°C]; and Rod 5 maxima [+0.66°C to +7.48°C] minima [-4.54°C to -0.26°C].

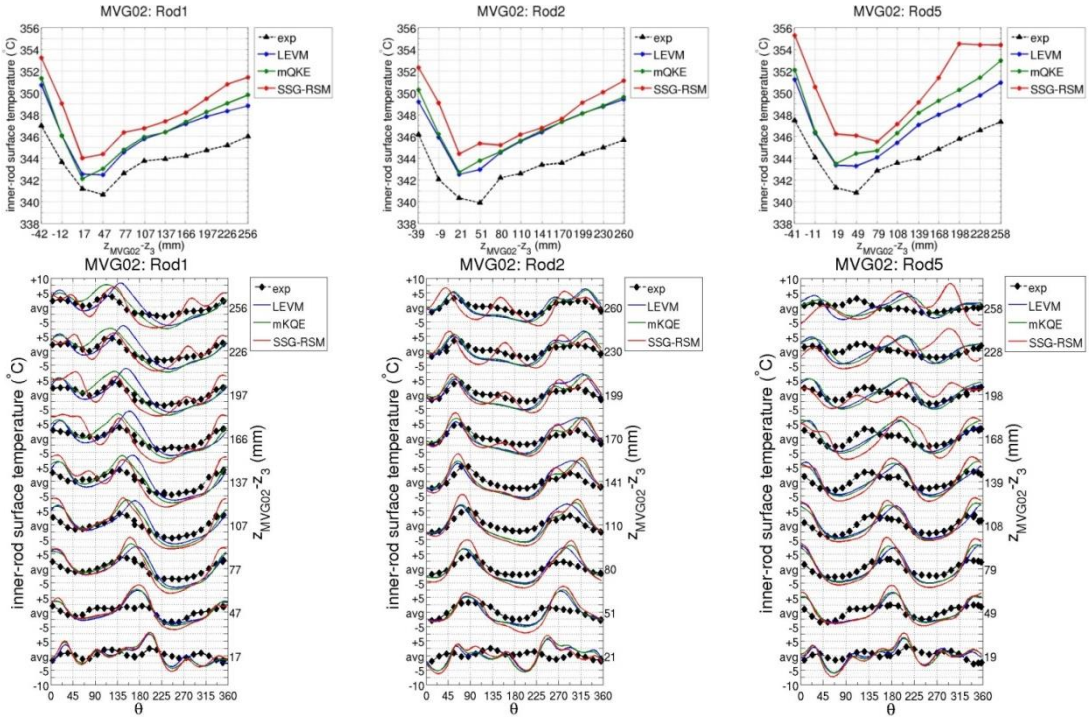

Figure 18 Axial (top column) and azimuthal (bottom column) distributions of rod wall inner-surface temperature (Rods 1, 2, and 5) along MVG02 wake region

5 CONCLUSION

Steady RANS CFD methodologies and CFD-code-to-experiment comparisons were presented for the MANIVEL-MVG and OMEGA-MVG rod bundle under isothermal and heated test conditions, respectively. Axial and global mesh size sensitivity studies identified reasonable mesh refinements for various regions of the SSG and MVG span types. CFD calculations adopted a sufficiently fine mesh and high-y+ wall function for CFD-code-to-experiment comparisons. This study requires the adoption of conjugate heat transfer for two reasons. First, accurate treatment of the thermal boundary condition, Joule heating (constant volumetric heat flux) through the rod cladding thickness, requires the cladding thickness to be resolve. Second, the rod inner-surface temperature was adopted for the thermal CFD-code-to-experiment benchmark comparison, thus conjugate heat transfer must be adopted in order to resolve and model conduction through the rod cladding thickness.

Examined turbulence models over predicted and slightly under predicted MVG and SSG pressure loss ratios, respectively. CFD-calculations for CFD-code-to-experiment benchmark comparisons produced comparable mean axial velocity (MVG and SSG spans), RMS axial velocity fluctuation (MVG span) profiles, and over-predicted rod inner-surface temperature profiles along the examined axial and azimuthal ranges. Even though rod inner-surface temperature was over-predicted, the temperature trend across the SSG was identified as a possible source of systematic error for examined CFD

methodologies. Furthermore, a relationship between secondary flow intensity and rod inner-surface temperature trend along the MVG wake region was suggested.

The SSG's main purpose in the NESTOR-MVG bundles is to stabilize the 5×5 rod array between consecutive MVGs. Differences in mean axial velocity profiles and lateral velocity vector fields between LEVM and anisotropic turbulence models (mQKE and SSG-RSM) indicated developing secondary flow structures in the SSG's far wake region. Thus, the mere inclusion of SSGs in the NESTOR MVG bundle introduces a basic limitation for validating CFD methodologies to a general PWR MVG bundle.

REFERENCES

1. Herr, W., Pröbstle, G. "Index matched flow measurements in rod bundles near grid spacers with swirl generators," *Laser Anemometry- Advances and Applications: Proceedings of the Second International Conference*, pp. 117-129, 1987.

2. Karoutas, Z., Gu, C.Y., Schölin, B. "3-D analyses for design of nuclear fuel spacer," *Proceedings of the Seventh International Meeting on Nuclear Reactor Thermal-Hydraulics*, pp. 3153-3174, 1995.

3. McClusky, H.L., Holloway, M.V., Conover, T.A., Beasely, D.E., Conner, M.E., Smith III, L.D., "Mapping of the lateral flow field in typical subchannels of a support grid with vanes," *ASME Journal of Fluids Engineering*, **125**, pp. 987-996, 2003.

4. Chang, S.K., Moon, S.K., Won, W.P., Choi, Y.D., "Phenomenological investigations on the turbulent flow structures in a rod bundle array with mixing devices," *Nuclear Engineering and Design*, **238,** pp. 600-609, 2008.

5. Yang, S.K., Chang, M.K. "Turbulent flow through spacer grids in rod bundles," *ASME Journal of Fluids Engineering*, **120**, pp. 786-791, 1998.

6. Shen, Y.F., Cao, Z.D., Lu, Q.G., "An investigation of crossflow mixing effect caused by grid spacer with mixing blades in a rod bundle," *Nuclear Engineering and Design*, **125,** pp. 111-119, 1991.

7. Connor, M.E., Baglietto, E., Elmahdi, A.M., "CFD methodology and validation for single-phase flow in PWR fuel assemblies," *Nuclear Engineering and Design*, **240**, pp. 2088-2095, 2010.

8. Yakhot, V., Or Orszag, S.A., Thangam, S., Gatski, T.B., Speziale, C.G., "Development of turbulence models for shear flows by a double expansion technique," *Physics of Fluids A: Fluid Dynamics*, **vol. 4 no. 7**, pp. 1510-1520, 1992.

9. Lee, J.R., Kim, J., Song, C.H., "Synthesis of turbulent mixing in a rod bundle with vaned spacer grids based on the OECD-KAERI CFD benchmark exercise," *Nuclear Engineering and Design*, **279,** pp. 3-18, 2014.

10. Bergeron, A., Chataing, T., Décossin, E., Garnier, J., Péturaud, P., Yagnik, S.K., "Design, feasibility, and testing of instrumented rod bundles to improve heat transfer knowledge in PWR fuel assemblies," *Proceeding of the 2007 International LWR Fuel Performance Meeting*, **1081,** pp. 62-68, 2007.

11. EPRI, "Computational fluid dynamics benchmark of high fidelity rod bundle experiments: industry round robin phase 2 – rod bundle with mixing vane grids," *Technical Report 3002005401*, pp 2-3 2-5 2-6 2-7 2-9 2-11 A3-A7, 2015.

12. Lemmon, E.W., McLinden, M.O., Friend, D.G., "Thermophysical properties of fluid systems" in *NIST Chemistry WebBook, NIST Standard Reference Database Number 69*, Eds. Linstrom, P.J., Mallard, W.G., National Institute of Standards and Technology, Gaitherburgs MD, 20899, http://webbook.nist.gov/chemistry/fluid/, 2015.

13. Daw, J.E., Rempe, J.L., Knudson, D.L., "Thermal properties of structural materials found in light water reactor vessels," *INL/EXT-09-16121*, **1**, pp. 4-5 - 4-8 and 5-8 - 5-11, 2009.

14. Jones, W.P., Launder, B.E., "The prediction of laminarization with a two-equation model of turbulence", *Int. J. Heat and Mass Transfer*, **15**, pp. 301-314, 1972.

15. Launder, B.E., Sharma, B.I. "Application of the energy dissipation model of turbulence to the calculation of flow near a spinning disc", *Letter in Heat and Mass Transfer*, **vol. 1, no. 2**, pp 131-138, 1974.

16. Baglietto, E., Ninokata, H., Misawa T. "CFD and DNS methodologies development for fuel bundle assemblies," *Nuclear Engineering and Design*, **236**, pp. 1503-1510, 2006.

17. Speziale, C.G., Sarkar, S., and Gatski, T.B., "Modeling the pressure-strain correlation of turbulence – an invariant dynamical systems approach," *J. Fluid Mechanics*, **227**, pp. 245-272, 1991.

18. CD-adapco, Inc., "Uer guide STAR-CCM+ version 9.04," *STAR-CCM+*, **9.04.009**, pp. 3384-3392 8802-8804, 2014.

19. Vonka, V., "Measurement of secondary flow vortices in a rod bundle," *Nuclear Engineering and Design*, **106**, pp. 191-207, 1988.